Normalized Raman Imaging for Studies of Tissue Physiology of the Kidney

Oh, S.[1,§,±]

Trim, W.V. [1,±]

Diakova, M. [1]

Petrova, K. [1]

Ichimura, T. [2]

Takakura, A. [2]

Karmakar, R. [3]

Nørrelykke, S.F. [3]

Peshkin, L. [1]

Bonventre, J.V. [2]

Kirschner, M. [1,*]

[1] Department of Systems Biology Department, Harvard Medical School, Harvard University. Boston, MA 02115, US.

[2] Renal Division, Brigham and Women's Hospital, Harvard Medical School. Boston, MA 02115, US.

[3] Image Analysis Collaboratory, Harvard Medical School. Boston, MA 02115, US.

[*] Corresponding Author: Marc@hms.harvard.edu.

[§] This author is now affiliated with the Department of Physics and the Department of Cellular Molecular Medicine at the University of California San Diego

[±] These authors contributed equally

Conflicts of interest:

M.K. and S.O. hold a patent for Normalized Raman Imaging (NoRI), US11971357B2, doi: 10.1073/pnas.2117938119.

Author Contributions:

Research design and conception: S.O., W.V.T., T.I., J.V.B., L.P., and M.K.

Primary data collection: S.O., W.V.T., T.I., A.T.

Data analysis and interpretation: S.O., W.V.T., M.D., K.P., T.I., A.T., J.V.B., R.K., S.F.N., L.P., and M.K.

Manuscript writing: S.O., W.V.T., M.D., and M.K.

Acknowledgements:

We would like to thank Dr. ChangHee Lee for his helpful assistance in providing the FiJi script for NoRI channel assembly. We would also like to thank Dr. Xili Liu, Dr. Avik Murkherjee, and Ang Li for their helpful assistance in maintaining the NoRI microscope.

Data availability:

All raw code is available at:

https://github.com/kirschnerlab/NoRI

https://github.com/HMS-IAC/nori

https://github.com/MDyakova/NORI_image_segmentation

https://github.com/MDyakova/NORI_feature_extraction

https://hms-iac.github.io/NoRI/

All raw image data are available at Zenodo: [*pending link*].

Abstract:
Histology is the cornerstone of clinical pathology and an essential tool for many areas of medicine. Nevertheless, conventional histological methods, which rely on fixation, embedding, sectioning, and staining, distort cellular architecture, extract key molecules such as lipids, and introduce variability that severely limits reproducibility. Here, we present Normalized Raman Imaging (NoRI), a form of stimulated Raman scattering applied to organ pathology. NoRI enables quantitative, label-free measurements of proteins and lipids at high spatial resolution. NoRI overcomes heterogeneous light scattering from homogeneous tissues by computationally correcting each signal by the combined Raman signals of protein, lipid, and water. This enables quantitative biomass measurements while preserving tissue architecture, thereby facilitating advanced analysis by convolutional neural networks and feature discovery. Here we apply NoRI to the mouse kidney, showing that such imaging can be used to accurately classify tubule types (median F1 [harmonic mean of precision and recall against manual annotation]=0.93), anatomical regions (F1=0.91), and biological sex (F1=0.97) from regions as small as 132.5µm². Under these circumstances, NoRI has revealed novel sex-specific features, including higher cytoplasmic lipid (+6.9mg/mL; p=0.028), nuclear protein (+26.3mg/mL; p<0.001), and capillary protein concentrations (+3.1mg/mL; p<0.001) in female tubules, along with differences in intracellular lipid droplet morphology. In a time-course model of acute kidney injury (AKI), NoRI captured dynamic changes in protein and lipid organization, most pronounced at day 2 post-injury (F1=0.97), and quantified recovery of brush border structures and lipid droplets over 25 days. Lipid measurements were particularly critical for the high accuracy of feature classification and discovery in AKI (F1=1.0). These results establish NoRI as a reproducible, high-resolution, and fully quantitative framework for tissue analysis and feature discovery, far surpassing conventional histology. By preserving tissue architecture and accurately quantifying lipids and proteins, NoRI provides a unique platform to explore and identify unknown biological phenomena in complex tissues, and present as a powerful diagnostic tool for histopathology.

Introduction:

Following the invention of the compound microscope by the Janssens in the late 16th Century, Marcello Malpighi and other physicians pioneered its use for the study of the micro-anatomy of organs(1). By the 19th Century, the modern field of histology had been born. For the succeeding two centuries, microscopy has been at the center of discovery in the biological and medical sciences and for the routine diagnosis of many pathologies, especially cancer. During this time, there were significant improvements in microscopes themselves, but arguably histopathology depended on parallel developments of highly effective means of fixation, embedding, sectioning, and staining. Today's standard approaches to modern histology are closely related to the technologies developed during the golden age of histology in the latter 19th Century(2). Such tools and methods were responsible for some of the greatest discoveries in biology and embryology sciences in the 19th and 20th Centuries. Today, routine clinical pathology still makes use of many of these same approaches, such as formaldehyde as a fixative, paraffin embedding and mechanical sectioning to visualize tissues, and hematoxylin and eosin staining, devised by Nicolaus Wissotsky in 1877. For a long time, it has been appreciated that these means of tissue preparation, though revealing discrete highly contrasting details of cell structure, such as of chromosomes on the mitotic spindle, nevertheless distort more subtle features, which are blurred by the harsh chemical treatments, which also distort cellular structures and extract components of living cells, such as lipids and water-soluble materials. There is also considerable variability in the methods themselves due to variations in dye batches and inconsistent lab practices. Compensating for this inconsistency and distortion is difficult, since no gold standard for comparison exists. Nevertheless, histopathology remains an important part of the armamentarium of both clinical practice and fundamental biology of multicellular animals.

To address the limitations of conventional histological approaches, particularly the complete absence of lipid information, we have recently developed a Normalized (stimulated) Raman imaging microscope with associated methods (NoRI)(3, 4). Stimulated Raman scattering microscopy (SRS) had previously been used to quantify cellular materials by Freudiger*, et al.* (5), particularly to reveal lipids

103 but its quantitative limitation by heterogeneous signal attenuation in thick tissue samples limited its
104 applicability(6). To overcome this, Oh*, et al.* (3) developed a normalization process that relied on an
105 additional channel for water. NoRI enabled precise determination of cell protein and lipid mass, at high
106 spatial resolution, in live or fixed tissues by computationally removing light scattering artefacts.
107 Furthermore, it was highly quantitative, a feature important for application of machine learning. With
108 NoRI, chemical composition (namely, protein [CH_3 bonds], lipid [CH_2 bonds], and water) is
109 automatically converted into absolute concentrations(3). This allows for absolute quantification of
110 cellular protein, lipid, and water; such calculations enable extraordinarily accurate cross-comparisons
111 of samples for feature identification. Consequently, NoRI data are unique not only due to their
112 quantitative nature or ability to visualize lipids but also owing to their un-disturbed view of preserved
113 structures. Nevertheless, detailed histopathology has not been explored in complex tissue specimens
114 using NoRI to date.

115 For performing a histopathological analysis using NoRI, we selected the kidney as a candidate organ.
116 The primary functions of the kidney, which Claude Bernard credited with maintaining the "milieu
117 interieur," include: 1. Blood filtration for waste removal, 2. Regulation of total body fluid balance, 3.
118 Metabolic blood acid-base balance, and 4. Regulation of blood pressure. The kidney is also optimal for
119 testing the suitability of NoRI for histopathology owing to its diverse array of distinct cell types
120 comprising the functional unit, or nephron, which has many subunits, as well as the vasculature and
121 interstitium. The kidney is also ideal since it is composed of distinct anatomical regions, including
122 cortex, and outer and inner medulla. Given the critical connection of the kidneys' own physiological
123 function to whole-body physiology, understanding of the microanatomy of the kidney is vital to
124 understanding both its physiology and how it regulates the physiology of the organism. More recently,
125 machine learning methods have attempted to advance kidney histopathology and have offered the
126 prospect of assisted diagnostics for clinicians and pathologists(7-9). Nevertheless, these methods are
127 severely limited by the high variability in the primary image data derived using traditional techniques.
128 As such, deep-level information related to lipids and microarchitecture is lost, and inconsistency is

129 introduced between samples, making the generation of robust models and discovery of generalizable
130 features difficult. Conventional histology, with its limited quantitative capacity and omission of lipids,
131 may never be able to recover subtle, detailed information needed for deep machine learning models
132 that would allow reliable diagnosis of kidney pathology.

133 As a first step to articulate a quantitative and minimally perturbed analysis of kidney microanatomy
134 we utilized quantitative, highly sensitive image data obtained from NoRI microscopy in healthy and
135 diseased mouse kidneys. The consistency of the new microscopic methods enabled an unprecedented
136 application of machine learning, based on absolute quantification of the protein and lipid signals.
137 Application of convolutional neural networks, a powerful form of machine learning, to the NoRI images
138 in the setting of kidney ischemia-reperfusion injury—a model of acute kidney injury—allowed us to
139 explore the potential sensitivity and reproducibility of NoRI for its application to histopathology and
140 feature discovery. These findings show how NoRI represents a unique tool to explore unknown
141 biological phenomena and provide a basis for advanced, automated histopathology in complex live or
142 fixed tissues.

143

144 **Methods and Materials:**

145 *Animals:*

146 Experiments on kidney anatomy and sex differences were performed on C57BL/6 mice, purchased
147 from Charles River Laboratories, which were housed at the Harvard Institutes of Medicine animal
148 facility. Unilateral ischemia reperfusion experiments were performed in male BalbC mice (*described*
149 *below*). Sixteen-week-old mice weighing 23.0–30.6 g (mean: 27.3 g) were used throughout. All animal
150 protocols were approved by the institutional animal care and user committee of the Harvard Medical
151 School.

152

153 Unilateral ischemia reperfusion surgery

154 Studies were performed according to the animal experimental guidelines issued by the Animal Care
155 and Use Committee at Brigham and Women's Hospital, Boston, USA. Male BalbC mice were obtained
156 from Charles River Laboratory and were allowed free access to water and standard mouse chow.
157 Animals were anesthetized with pentobarbital sodium (60mg/kg body weight, intraperitoneally) prior
158 to surgery. Analgia was provided with Ethiqa XR (3.25mg/kg). The mice were placed on a heating pad
159 and body temperatures were maintained between 36.8-37.2ºC throughout the procedure. The kidney
160 was exposed via flank incisions, and unilateral renal ischemia was induced by clamping left renal
161 pedicle with non-traumatic microaneurysm clamps (Roboz, Rockville, MD, USA) for 20 min. The kidneys
162 were returned to the original place, and the incisions were temporarily closed during ischemia. After
163 the clamps were removed, reperfusion of the kidney was visually confirmed. The muscle layer was
164 closed using absorbable sutures and the skin incision was closed using sterile staples. One millilitre of
165 pre-warmed 0.9% normal saline was administered after surgery. The mice were kept on a warm pad
166 until fully recovered, then returned to their cages. Moist food pellets were placed on the bedding for
167 easy access, and animals were monitored twice daily.

168

169 *Kidney resection and fixation:*

170 Following sacrifice, mice were perfused with chilled (4ºC) phosphate buffered saline (PBS) containing
171 10 U/mL sodium heparin. Kidneys were then resected and cut in half, placed into 5 mL 4 %
172 formaldehyde in PBS (Thermo-Fisher Scientific; MA, US), and stored at 4ºC for 24 hours. Following
173 fixation, samples were washed twice with chilled PBS and were stored in PBS containing 0.02 % sodium
174 azide (Sigma-Aldrich; MilliporeSigma. MA, US) at 4ºC for no longer than one-week before analysis.

175

176 *Kidney slices and immunofluorescence processing:*

177 Whole-kidneys were removed from storage and placed into mounting cylinders compatible with the
178 Precisionary ZF-310-0F Compresstome® (Precisionary Instruments LLC.; MA, US) containing 2 %
179 agarose diluted in distilled water (pre-heated to 50ºC) (EZ Pack Agarose™; Benchmark Scientific, Inc.;
180 NJ, US). All buffers used were filtered through a 0.22 µm filter (Corning®; AZ, US) prior to use.
181 Constructs were then kept at 4ºC for 30 minutes to harden the agarose-sample construct. Samples
182 were next placed into the Compresstome® and cut into 120 µm slices at speed setting 4, oscillation
183 setting 2. Individual tissue slices were then placed into ~2 mL chilled PBS (0.02 % sodium azide) within
184 a 12-well plate (VWR International, LLC; NJ, US). Samples were then placed into PBS containing 5 %
185 normal donkey serum (Jackson ImmunoResearch Laboratories Inc.; PA, US) containing 0.02 % sodium
186 azide overnight at 4ºC with gentle rocking. Blocking solution was removed and replaced with PBS
187 containing 0.02 % sodium azide at room temperature with gentle rocking for 20 minutes, repeated
188 three times; these procedures were found to have no influence on the quantification of protein or lipid
189 by NoRI (**Supplementary Fig. 1**).

190 After washing, the wash buffer was replaced with primary antibodies in tandem in PBS containing 0.02
191 % sodium azide for combinations of the following antibodies; Rat anti-mouse endomucin (1: 200) (sc-
192 65495; Santa Cruz Biotechnology, Inc.; CA, US), sheep anti-mouse uromodulin (1: 200) (T0850-02B;
193 USBiological Life Sciences; MA, US), and rabbit anti-mouse aquaporin 2 (1: 200) (29386-1-AP;
194 Proteintech, ChromoTek GmBH; IL, US). Samples were incubated in primary antibody cocktail for 24
195 hours at room temperature with gentle rocking. Primary antibody cocktail solution was then removed
196 and replaced with PBS containing 0.02 % sodium azide for 30 minutes at room temperature with gentle
197 rocking to wash. This wash was repeated 4–6 times.

198 For samples where lotus tetragonolobus lectin (LTL) labelling of brush border was performed following
199 primary antibody incubations, tissue sections were placed into PBS spiked with 10 µM calcium chloride
200 and avidin blocking solution (Vector Laboratories; CA, US) according to manufacturer
201 recommendations for 30 minutes at room temperature with gentle rocking. From this point on, all
202 buffers were spiked with 10 µM calcium chloride according to manufacturer recommendations for
203 samples where LTL was labelled. Samples were then washed at 20-minute intervals for 60 minutes
204 total in PBS containing 0.02 % sodium azide. After washing, samples were placed into PBS (+10 µM
205 calcium chloride) and biotin blocking solution (Vector Laboratories; CA, US) according to manufacturer
206 recommendations for 30 minutes at room temperature with gentle rocking. Samples were then
207 washed at 20-minute intervals for 60 minutes total in PBS containing 0.02 % sodium azide. Samples
208 were then placed into biotinylated LTL antibody solution (1: 250) (B-1325-2; Vector Laboratories, Inc.;
209 CA, US) in PBS (+10 µM calcium chloride) containing 0.02 % sodium azide for 24 hours at room
210 temperature with gentle rocking. Following LTL incubation, samples were washed in PBS (+10 µM
211 calcium chloride) containing 0.02 % sodium azide for 60 minutes 4–6 times at room temperature with
212 gentle rocking. Next, samples were incubated in secondary antibody cocktail solution for 24 hours at
213 room temperature with gentle rocking, in darkness, in PBS (+10 µM calcium chloride) containing 0.02
214 % sodium azide with combinations of the following antibodies; AffiniPure donkey anti-sheep Alexa
215 Fluor® (AF)488 (1: 250) (Jackson ImmunoResearch Laboratories Inc.; PA, US), AffiniPure donkey anti-

216 rabbit AF647 (1: 250) (Jackson ImmunoResearch Laboratories Inc.; PA, US), AffiniPure donkey anti-rat
217 DyeLight™ (DL)405 (1: 250) (Jackson ImmunoResearch Laboratories Inc.; PA, US), and streptavidin
218 AF594 (1: 250) (ThermoFisher Scientific, Inc.; MA, US). Secondary antibody cocktail solution was
219 removed and replaced with PBS (+10 µM calcium chloride) containing 0.02 % sodium azide for 30
220 minutes at room temperature, in darkness, with gentle rocking, repeated 4–6 times.

221 After washing, samples were mounted onto glass slides (Superfrost® Plus VWR MicroSlides; VWR
222 International LLC.; PA, US) with a small amount (~75 µL) of anti-fade mounting solution containing 0.2
223 % propyl-gallate (Sigma-Aldrich; MA, US) diluted in 0.8 % fully deuterated dimethylsulfoxide (DMSO;
224 MilliporeSigma; MA, US) in PBS (+10 µM calcium chloride) containing 0.02 % sodium azide. The
225 deuterated form of DMSO was used so as not to contribute to the NoRI quantitation of the protein
226 methyl groups. Number 1.5 micro cover glass slides (VWR International, LLC.; PA, US) were used to
227 cover samples and slides were sealed using clear nail polish. Samples were stored at 4ºC in darkness
228 in a humidified container until imaging.

229

230 *Fluorescence microscopy and normalized Raman imaging (NoRI):*

231 Microscopy imaging and quantitation was performed on an Olympus FV3000 using Fluoview (Olympus;
232 Tokyo, Japan) and MatLab™ (MathWorks; CA, US). Immunofluorescence imaging was used for cell-type
233 and tubule identification and for identification of markers of cellular stress. The immunocytochemistry
234 was followed by NoRI imaging for protein and lipid quantification. All images were taken using a water
235 immersion 60x 1.2NA objective lens (Evident-Scientific) and an oil immersion 1.4NA condenser lens,
236 where each pixel was equivalent to 414nm for both NoRI and immunofluorescence imaging.

237 Protein and lipid concentrations were calculated from SRS images using NoRI as previously
238 described(3, 4). Briefly, SRS images at 2853 cm^{-1}, 2935 cm^{-1}, and 3420 cm^{-1} bands (corresponding to
239 the methylene- and methyl-groups, and water characteristic vibrational bands, respectively) were

240 acquired from live or fixed cells using a custom-built spectral-focusing femtosecond SRS microscope.
241 This microscope was constructed using synchronized femtosecond pulse lasers for the Pump and
242 Stokes beams. A pair of dense flint (DF) glass rods chirped the pulses. An electro-optical modulator
243 (EOM) modulated the amplitude of the Stokes beam at 20 MHz. A retro-reflector prism mounted on a
244 motorized delay was adjusted to control the overlap of the Pump and Stokes beams. The Pump and
245 Stokes beams, combined by a dichroic mirror (DM), were focused on the sample by the objective lens.
246 Images were acquired by point-scanning using a pair of galvanized mirrors (scan mirror). After passage
247 through the stimulated Raman scattering at the sample plane, the Pump beam was collected by a high
248 numerical aperture condenser lens, selected by a short pass filter (SF), and its intensity was measured
249 by a high-speed photodetector. The three SRS images were spectrally unmixed into protein, lipid, and
250 water components using reference spectra measured from bovine serum albumin solution in water,
251 dioleoyl-phosphocholine solution in per-deuterated methanol, water, and per-deuterated methanol.
252 Unmixed images of protein, lipid, and water components were converted to the absolute
253 concentration by using the sum of the three components as the normalization reference at each pixel.
254 A representative region within each kidney that were imaged is presented in **Supplementary Fig. 2**.

255

256 *Data analysis and image segmentation:*

257 All images were processed by customized codes in Matlab™ (Mathworks) or ImageJ and FiJi (National
258 Institute of Health). NoRI and immunofluorescence images were stitched together using the
259 Grid/Collection stitching plugin for Fiji(10), and stacked into one multi-channel image using a custom
260 macro for FiJi.

261 This study utilized an automated pipeline to quantify protein and lipid concentrations within the
262 cytoplasm of individual kidney tubules. The approach involved three key steps: segmentation,
263 classification, and measurement. A detailed description of this methodology, along with its validation

and application, is also available in Karmakar, Trim, Kirschner and Noerrelykke (11). Segmentation was performed using a combination of classical image processing, deep learning and machine learning techniques, including the Segment Anything Model (SAM) for tubule segmentation(12); with the exception of glomeruli, which were hand-segmented. Post-processing steps, such as morphological operations and expert validation, were applied to refine segmentation accuracy. For comparison with SAM, a YOLOv8-based object segmentation model(13) was also fine-tuned to detect kidney tubules in NoRI images using annotated data derived from the protein and lipid signals. Fine-tuning was conducted on 640×640-pixel image crops, batch size of 16 with 200 epochs (iterations). Early stopping (where learning ends once a model's metrics do not continue to improve further) after 30 epochs was performed. Data augmentation was applied to ensure robustness, using horizontal/vertical flips, random rotations, brightness/contrast adjustments, and affine transformations. All images were normalized using standard ImageNet mean and standard deviation values(14). The model was configured for single-class detection and fine-tuned using the Ultralytics YOLO implementation(13). Tubule classification was performed using Ilastik's(15) object classifier, leveraging immunofluorescence markers (LTL, UMOD, and AQP2) to distinguish tubule types.

Nuclei were segmented using a U-Net model fine-tuned on manually labelled binary masks(16). The input data consisted of 640×640 patches from the protein channel, and corresponding nuclei masks were manually annotated based on visible nuclear morphology. The U-Net architecture followed a standard encoder–decoder design with skip connections and was implemented in PyTorch(17). Fine-tuning was conducted for up to 200 epochs, with a batch size of 8, and learning rate of 0.0001, where an epoch represents one full pass through the dataset, batch size represents the number of samples processed before the model updates its weights, and learning rate represents a step size for adjusting model weights during optimization. For fine-tuning, we used the binary cross-entropy loss and the Adam optimizer(18). Early stopping was applied after 30 epochs without validation improvement. The training data underwent geometric (i.e., rotations, cropping, scaling changes) and photometric (i.e., altered brightness/contrast, noise addition, blurring) augmentations, and all images were normalized

to ImageNet statistics. We chose the model with the best Dice score—where Dice score represents the similarity between two segmented polygons, calculated as twice the intersection area divided by the sum of the areas of the two polygons—as a final model(16). Brush borders were segmented using a U-Net model fine-tuned(16) on manually labelled binary masks. The input data consisted of tubule images of 128×128 patches from the protein channel and lipid channels, and corresponding brush border masks were manually annotated based on visible brush border morphology. The U-Net architecture followed a standard encoder–decoder design with skip connections and was implemented in PyTorch(17). Fine-tuning was conducted using the same parameters as for nuclei. To identify luminal regions within segmented tubules, hierarchical clustering to low-intensity pixels in NoRI images was applied. Pixels were extracted using intensity values below a predefined threshold for each segmented tubule from the maximum projection of all imaging channels. These pixels were clustered using agglomerative hierarchical clustering with a Euclidean distance threshold of 5 pixels. Clusters containing fewer than 75 pixels were discarded to reduce noise. The remaining clusters generated binary masks representing lumen locations within the tissue(19). Nucleoli were segmented using a U-Net model fine-tuned on manually labelled binary masks(16). The input data consisted of nuclei images of 32x32 patches from the protein channel and lipid channels, and corresponding nucleoli masks were manually annotated based on visible morphology. The U-Net architecture followed a standard encoder–decoder design with skip connections and was implemented in PyTorch(17). Fine-tuning was conducted using the same parameters as for nuclei.

Protein and lipid concentrations were quantified by measuring pixel intensities within the cytoplasm, obtained by subtracting the segmented nuclei, nucleoli, lumen, and brush border regions from the tubule mask. Intensity values were converted to concentrations using established conversion factors for protein and lipid. The resulting measurements provided insights into the spatial distribution of these biomolecules across different tubule types.

Feature-based classification, feature extraction, and interpretability analysis

ResNet50 convolutional neural network(20), trained on ImageNet, was used to identify regions of interest in NoRI images. The model's final fully connected layer (where every neuron is connected to every neuron in the neural network's previous layer) was replaced with a new layer corresponding to the number of classes (e.g., cell types, sex, ischemic timepoint) in the dataset. Input images were organized into folders labelled by class and divided into training and validation sets. Image tiles were resized and randomly augmented through horizontal and vertical flips, rotations (0–270°), and random crops. All images underwent normalization using ImageNet's mean and standard deviation. For model fine-tuning, we utilized cross-entropy loss and the Adam optimizer (learning rate = 0.0005) for up to 25 epochs, evaluating performance using accuracy and macro-averaged F1-score (a performance metric on an ascending scale of 0–1 for classification performance calculated as the harmonic mean of precision and recall [$2/(\text{precision}^{-1} + \text{recall}^{-1})$]). The best-performing model weights (i.e., those closest to 1) were saved.

To extract high-level image features (determined by the neural network) and visualize class-specific patterns (i.e., features that determine the class) in NoRI images, fine-tuned ResNet50 models were employed and activations (the output signals produced by a layer of a neural network after it applies its transformation to the input) were retrieved from the penultimate average down sampling layer. Images were transformed using standard normalization and resizing procedures before being passed through the network in evaluation mode. The resulting feature vector was saved and used for dimensionality reduction and visualization with UMAP for each tile. In parallel, Grad-CAM (Gradient-weighted Class Activation Mapping(21)) was applied to layers 2, 3, and 4 of the ResNet architecture to produce class-discriminative heatmaps that highlight image regions most relevant to the model's predictions. These heatmaps were overlaid on grayscale representations of the original inputs to facilitate biological interpretation. UMAP plots and Grad-CAM overlays were generated for validation samples to promote qualitative and quantitative assessment of class differences.

340 Following feature identification by ResNet50, to identify and quantify luminal regions and lipid droplets
341 within segmented tubules and microvasculature regions, hierarchical clustering to low-intensity pixels
342 in NoRI images was applied. Pixels were extracted using intensity values below a predefined threshold
343 for each segmented tubule from the maximum projection of all imaging channels.

344 All code and materials used for image processing can be accessed at: https://github.com/HMS-
345 IAC/nori, https://github.com/MDyakova/NORI_feature_extraction and
346 https://github.com/MDyakova/NORI_image_segmentation. A schematic summary of
347 segmentation and machine learning analysis pipelines is presented in **Supplementary Fig. 3**.
348

349 *Histological preparation and analysis:*

350 A single section of a kidney from five healthy male and five healthy female mice were fixed as described
351 above and were dehydrated, paraffin-embedded, and stained with haematoxylin and eosin by
352 INVIVOVEX LLC. (MA, US). Slides were imaged at 60x magnification on an Olympus slide view VS200.

353

354 *Statistical analysis*:

355 All statistical analyses and graphical representations were performed and produced using MatLab™
356 and GraphPad Prism (MA, US). MatLab scripts are accessible from:
357 https://github.com/kirschnerlab/NoRI. Comparisons between variables, where normally
358 distributed were performed using student's *t*-tests. Where non-normally distributed, Mann-Whitney
359 *U* non-parametric equivalents were used. Cumulative distribution analysis was performed using
360 Kolmogorov-Smirnov tests. For analysis of time-course results, Analysis of Variance (ANOVA) tests
361 were performed, with Bonferroni post-hoc corrections applied. For analysis of ≥3 groups, one-way
362 ANOVA was performed, with Dunn's post-hoc corrections applied. Distribution of raw protein and

363 lipid concentrations between groups were compared using Kruskal-Wallis tests, with Dunn's post-hoc
364 corrections applied. Effect sizes were estimated using Cohen's *d* calculations throughout. Specific
365 uses of each statistical test are detailed in the respective figure legends. Statistical significance was
366 set at $p \leq 0.05$.

367 **Results:**

368 To establish the potential of NoRI microscopy for exploring tissue biology we first needed to establish
369 its accuracy in measuring proteins and lipids in a well-studied organ under varying conditions. After
370 examining several organs, we chose the intact mouse kidney. We studied the kidney under three
371 physiological or pathophysiological differences: female *versus* male, anatomical variation in the various
372 tissues and cell types in the kidney itself, and the injury and recovery after ischemia-reperfusion injury
373 induced by cessation of renal blood flow followed by reperfusion. At the same time, as we began to
374 appreciate the power of this data set, we experimented with various machine learning methods for
375 analysing NoRI images to measure changes in cells and tissues with known levels of confidence.

376 Samples were imaged by placement between a water immersion 60x 1.2NA objective lens (Evident-
377 Scientific) and an oil immersion 1.4NA condenser lens, where each pixel equated to 414nm for both
378 NoRI and immunofluorescence imaging. A representative kidney section imaged by NoRI is presented
379 in **Fig. 1A**. A single tile (212µm^2) image of NoRI and the corresponding immunofluorescence image is
380 presented in **Fig. 1B**. From such images we derived a mask (i.e., segmented region of interest) of kidney
381 tubules and other structures. A representative tubule structure and a corresponding sub-structure
382 mask is also presented for this same region (**Fig. 1B**). Representative examples of the segmentation of
383 nucleoli are presented in **Supplementary Fig. 4**, and representative images of all image channels and
384 segmentation layers are presented in **Supplementary Fig. 5**. We found that we could fine-tune image
385 models that would parse out tubules, lumen, nuclei, and brush border from the NoRI images, by using
386 a combination of Segment Anything Module (SAM)(12) (for tubules) and YOLO(13) (all remaining sub-
387 structures) fine-tuned against manual segmentation of tubules. Both SAM and YOLO had high mean
388 average precision scores (a single metric that summarizes a model's ability to correctly classify and
389 localize specific objects [e.g., a tubule] across all classes and confidence thresholds, against a gold-
390 standard [e.g., hand-segmented tubules]) for tubule and nuclei segmentation (**Fig. 1C**). We ascertained
391 the variability in cytoplasmic protein and lipid concentrations in proximal tubules (LTL+), distal tubules
392 (UMOD+), and connecting tubule and collecting ducts (AQP2+) in kidney slices from the Midpole

393 region of eight kidneys from four male and four female C57BL/6 mice (**Fig. 1D**). We found that tubule
394 types generally clustered based on their average cytoplasmic protein and lipid concentrations for
395 collecting ducts (Protein: 138.5±19.7 and Lipid: 40.2±13.1mg/mL), proximal tubules (Protein:
396 194.3±18.4 and Lipid: 52.2±9.5mg/mL), and distal tubules (Protein: 170.8±16.1 and Lipid:
397 62.4±10.3mg/mL) (**Fig. 1D**). These results also demonstrated the similarity of tubule cytoplasmic
398 concentrations across animals. Quantification of nuclear protein concentrations for different tubule
399 types and brush border protein/lipid in proximal tubules, and protein and lipid concentrations within
400 the glomeruli is presented in **Fig. 1E**. We observed that nuclei constitute 12.9±4.7% of the tubule area
401 but contained negligible quantities of the lipid within the cell. We also found differences in nuclear
402 protein concentration between tubule types that was statistically significant (134.7±19.3 *versus*
403 166.8±20.3 *versus* 130.7±22.4mg/mL for collecting ducts, proximal tubules, and distal tubules,
404 respectively; $p \leq 0.0001$; **Fig. 1E**). When we took all segmented tubules (not segregated by sub-types),
405 without immunofluorescence channels and processed them through ResNet50, the deep-
406 convolutional neural network (CNN) pipeline, we found NoRI+CNN analyses had the strongest
407 performance for tubule type prediction (mean ± SD F1-score: 0.93 ± 0.04; **Fig. 1G**). By comparison,
408 NoRI protein/lipid data, geometric features (*listed in* **Supplementary Table 1**), or a combination of both
409 were less powerful predictors of tubule type (F1-scores: 0.62±0.10, 0.58±0.13, and 0.67±0.12,
410 respectively; **Fig. 1G**). The impressive UMAP representation of tubule types predicted by NoRI+CNN is
411 presented in **Fig. 1H**.

412 Having found that different tubule types possessed different protein and lipid densities, we asked
413 whether protein and lipid concentration of cells in the kidney vary depending on their anatomical
414 location within the organ. To address this question, we took a section of kidney from three different
415 anatomical regions, namely Rostral pole, Midpole, and Caudal pole portions of both left and right
416 kidneys from two male mice and fine-tuned a ResNet50 pipeline on a sub-section of these images (**Fig.
417 2A**). The Caudal pole region had the highest F1-score for prediction (0.91±0.06; **Fig. 2B**), followed by
418 the Rostral pole (F1-score: 0.79±0.14) and Midpole (F1-score: 0.58: 0.58±0.25) (**Fig. 2B**). We also

419 identified statistically significant differences between all three anatomical regions for cytoplasmic
420 protein, and between all regions, except for Rostral pole and Midpole (p=0.123; **Fig. 2E**), for lipid
421 concentrations across tubules with highest cytoplasmic protein concentrations present in Caudal pole
422 sections (Protein: 158.4±29.5 and Lipid: 49.9±11.5mg/mL), whereas Midpole and Rostral pole were
423 similar across protein and lipid cytoplasmic concentrations ([Rostral pole] Protein: 134.6±21.0 and
424 Lipid: 43.1±9.0mg/mL, and [Midpole] Protein: 136.6±20.8 and Lipid: 42.6±9.0mg/mL)(*ANOVA*: all
425 p≤0.0001; **Fig. 2D, Fig. 2E** and **Supplementary Fig. 6**). These differences were further supported by
426 medium-to-high effect sizes when comparing distinct tubule types between Rostral pole *versus* Caudal
427 pole (d=0.63–1.21) and Midpole *versus* Caudal pole (d=0.88–1.76), but with less distinction between
428 Rostral pole and Midpole portions (d=0.27–0.99) (**Supplementary Fig. 6**). We also observed a
429 significant downward trend in proximal tubule cytoplasmic protein and lipid concentrations from
430 cortex to medulla in the Midpole region (r^2>0.281, p<0.0001; **Supplementary Fig. 7**). We did not
431 identify any significant differences between regions from left and right kidneys (F1=0.58; *data not*
432 *shown*).

433 We used the ResNet50 pipeline fine-tuned on different kidney regions to identify structural features
434 that might distinguish between regions (representative examples presented in **Fig. 2F**). These analyses
435 identified protein concentrations in spaces between tubules where the tissue microvasculature
436 resides—which we will term, "microvasculature." These represent the microvasculature of the kidney
437 and are a key distinguishing feature between regions, where the highest protein concentration was
438 found in Caudal pole sections (100.5±29.4mg/mL; p<0.0001), while Midpole and Rostral pole were
439 similar (77.2±22.3mg/mL and 78.3±21.2mg/mL, respectively; p>0.999)(**Fig. 2G**). We also found lipid
440 droplet concentration and size were significantly different between regions (p≤0.0001). Specifically,
441 Caudal pole exhibited highest lipid droplet concentration (84.7±22.9mg/mL), followed by Rostral pole
442 (75.4±22.0mg/mL) and Midpole (66.5±15.6mg/mL)(**Fig. 2H**). Conversely, lipid droplet size was
443 substantially larger in the Midpole (278±418 pixels) compared to Rostral or Caudal pole regions, which
444 were similar, on average (61±193 and 67±98 pixels, respectively) (**Fig. 2I**).

445 After confirming that NoRI combined with CNNs can predict tubule type and anatomical location of
446 tubules in a single kidney, we next turned our focus on examining sexual dimorphism, using four male
447 and four female C57BL/6 mice. We analyzed the cytoplasmic protein and lipid concentrations to
448 characterize broadly the differences between sexes (**Fig. 3A**). Cytoplasmic protein in LTL+ proximal
449 tubules—specialized in resorption of substances back into the bloodstream—was significantly higher
450 in female mice (256.9±6.9mg/mL), on average than for males (245.5±3.2)(p=0.029; **Fig. 3B**).
451 Furthermore, cytoplasmic lipid content was between 6.5–7.3mg/mL more concentrated in female
452 mice across all tubule types analyzed (p≤0.028; **Fig. 3C**). There were no differences between number
453 of tubules between sexes (p≥0.767; **Supplementary Fig. 8**). To probe more deeply into the localization
454 and features underpinning sex differences in mouse kidneys in NoRI images, we fine-tuned image tiles
455 of varying sizes from 40–320 pixels in size (~16.5–132.5µm^2, ranging from a single cell to several
456 tubules per image) to determine what type of input data in the ResNet50 pipeline best captured the
457 differences (**Fig. 3D**). We found a tile size of 320 pixels (132.5µm^2) achieved remarkable F1-scores for
458 predicting the sex of a given tubule, likely due to capturing larger regions of tubules and other
459 structures, though all image tile sizes worked to some degree, with high accuracy to predict the sex of
460 a tubule (average F1-scores: 0.82–0.97; **Fig. 3E**, **Supplementary Fig. 9**). We next explored what were
461 the actual features that ResNet50 that accounted for the sexual dimorphism (**Fig. 3G**). These analyses
462 revealed that the level of nuclear protein and the relative abundance of protein to lipid in the
463 microvasculature region were both significantly greater in females (+26.3mg/mL and +19.5%,
464 respectively; p≤0.001; d=0.82–0.83; **Fig. 3H** and **I**). The concentration of lipid and the size of the lipid
465 droplets were similarly significantly higher in females (+11.65mg/mL and +7.12µm^3, respectively;
466 p≤0.001; d=0.62–0.63; **Fig. 3J** and **K**). We also compared our ability to determine sex in the kidney with
467 conventional histological methods (H&E staining) against our combination of NoRI plus machine
468 learning analyses (**Supplementary Fig. 10**). We found that although sex could be reliably determined
469 from H&E images using ResNet50 (presumably due to the relative importance of protein over lipid as
470 shown by NoRI), the staining inconsistencies, lack of quantitative data, and disruption of tissue

471 architecture in H&E staining failed to register finite/smaller (e.g., sub-cellular-sized) features that could
472 distinguish males from females (i.e., at layers 2 and 3 of the ResNet50 output). Instead, activation maps
473 presented in **Supplementary Fig. 10** highlight sex discrimination was largely focused on macro-
474 structures such as entire tubule bodies, rather than sub-cellular structures/regions. This admittedly
475 unusual metric suggests that NoRI can better distinguish subtle differences in structure than H&E
476 staining and is much more quantitative, allowing for a direct measurement of such structures that are
477 normally lost due to staining variability sample-to-sample, or micro-architectural disturbance from the
478 extensive processing required by conventional histology protocols.

479 Given the success of NoRI in predicting tubule type, anatomical location, and the sex of a tubule simply
480 from structural and chemical composition (protein and lipid mass density) we applied NoRI and
481 convolutional neural networks to better understand kidney dysfunction, in a model of transient
482 unilateral ischemic-reperfusion injury (IRI). This model of acute kidney ischemia, caused by temporary
483 occlusion of the renal artery and vein of one kidney, leaving the other as a contralateral control, is a
484 common model for acute kidney injury (AKI)(22). When due to ischemia, AKI is characterized by oxygen
485 deprivation to inflammation, oxidative stress, renal damage, and recovery which can be "adaptive"
486 with few if any long-term consequences, or "maladaptive" resulting in incomplete repair with tissue
487 scarring/fibrosis (22). As such, this model represents a powerful means of exploring both kidney
488 damage and repair, as commonly occurs in human AKI.

489 In this AKI model, where occlusion occurred for only 20 minutes, we first performed a time course
490 analysis of signs of dysfunction and repair across collecting ducts, distal and proximal tubules. We
491 observed no change in tubule numbers between contralateral control and IRI kidneys at each time
492 point (**Supplementary Fig. 11**). We next analysed the cytoplasmic protein and lipid concentrations of
493 tubule types at each time point post-IRI and found that proximal and distal tubule cytoplasmic lipid
494 concentrations showed changes during the recovery period post-IRI (+6.3mg/ml from day 1 to
495 +8.3mg/mL at day 25 post-IRI, respectively). There were significant reductions in proximal tubule and

496 distal tubule lipid concentrations between groups specifically at day 2 post-IRI (52.9±0.6mg/mL *versus*
497 46.2±0.2mg/mL, and 61.3±2.2mg/mL *versus* 47.0±3.3mg/mL for proximal and distal tubule
498 cytoplasmic lipid concentration in contralateral control *versus* IRI kidneys at day 2 post-IRI,
499 respectively; two-way ANOVA: $p \leq 0.037$; **Supplementary Fig. 12**). We next explored the time course
500 relative to the contralateral control. We took NoRI images from days 1, 2, 5, and 25 post-IRI for both
501 contralateral control and ischemic kidneys and followed the time course of structural changes in kidney
502 dysfunction and repair following the ischemic injury (**Fig. 4A**). In support of the above findings in
503 **Supplementary Fig. 12**, we found the greatest difference between contralateral control and IRI (F1-
504 score: 0.97±0.04) at day 2 post-IRI (**Fig. 4B**). Days 1 and 5 post-IRI displayed similar degrees of
505 separation (F1-scores: 0.77–0.85; **Fig. 4B**). By day 25 post-IRI the distinction between and ischemic
506 kidneys was very much reduced (F1-score: 0.58; **Fig. 4B**). These changing properties were also
507 reflected in the spatial separation between contralateral control and ischemic tubules in **Fig. 4C–E**, but
508 the separation of clusters was not visible at day 25 post-IRI (**Fig. 4F**). We characterized the structural
509 changes imposed by IRI in contralateral control and ischemic kidneys over time to better understand
510 the underlying biological manifestations of AKI. On day 1 post-IRI, there were significant difference in
511 the microvasculature protein (96.4±25.6mg/mL *versus* 113.0±29.7mg/mL for contralateral control
512 *versus* IRI, respectively; $p \leq 0.001$; d=0.61–0.67; **Fig. 4J**), possibly reflective of vascular congestion. On
513 day 2 post-IRI, lipid droplet concentration was significantly lower in ischemic relative to contralateral
514 control kidneys (92.8±22.7mg/mL *versus* 76.8±25.8mg/mL; $p<0.001$), whereas brush border lipid
515 concentration was significantly greater in ischemic kidneys ([median±SEM] 30.7±0.4mg/mL *versus*
516 35.7±0.4mg/mL; $p<0.001$; **Fig. 4K**), however, effect size calculations revealed no effect (d=0.02) at day
517 2 post-IRI (**Fig. 4K**). On day 5 post-IRI, microvasculature protein concentration was also significantly
518 higher in ischemic kidneys (89.0±23.3mg/mL *versus* 110.1±28.0mg/mL for contralateral control *versus*
519 IRI, respectively; $p<0.001$; d=0.84; **Fig. 4L**), while lipid droplet size was significantly (but with small
520 effect), elevated in ischemic kidneys ($p<0.001$; d=0.26; **Fig. 4L**).

521 We anticipated using the contralateral (unligated) kidney as an internal control for the IRI experiment.
522 However, we were aware that the undisturbed contralateral kidney might have suffered an added
523 burden for having to both undertake the function of two kidneys, as well as being exposed to a post-
524 ischemic milieu of stress and damage from response molecules released by the ligated kidney. Thus,
525 we next turned our attention to detecting the effects of IRI on the unligated contralateral control
526 kidney and in ischemic kidney in isolation, over time (**Fig. 5A**). There were, in fact, significant changes
527 over time within both the contralateral control and ischemic kidneys over time (F1-score: 0.77–0.99;
528 **Fig. 5B**), suggesting the contralateral control kidney also exhibits substantial temporal responses post-
529 IRI. Specifically, distinct clustering between days 1 *versus* 2 and days 5 *versus* 25 was apparent in the
530 contralateral control kidney data (**Fig. 5C** and **E**). Indeed, this separation in the contralateral control
531 kidney UMAP clustering was similar to the distinct clustering found between timepoint post-IRI in the
532 ischemic kidneys (**Fig. 5F–H**). Using ResNet50 CNN analyses on the quantitative, undisrupted NoRI
533 images of kidneys we could easily detect changes in both contralateral control and ischemic kidneys
534 post-IRI (*representative images presented in* **Fig. 5I**). We found the concentration of protein within the
535 tubule lumen (representative of a pathological 'protein plug') increased from 30.8±19.3mg/mL to
536 39.9±25.0mg/mL, in contralateral control kidneys, and decreased from 37.1±24.2mg/mL to
537 34.7±22.8mg/mL from day 1 to day 25 post-IRI in ischemic kidneys (**Fig. 5J**), but was not entirely absent
538 by day 25 post-IRI. Lipid droplet concentrations also increased from 88.0±31.2mg/mL to
539 104.3±27.7mg/mL, in contralateral control kidneys, and from 93.8±32.9mg/mL to 94.9±26.4mg/mL
540 from day 1 to day 25 post-IRI in ischemic kidneys (**Fig. 5K**). Finally, we found brush border lipids also
541 increased from 35.4±11.2mg/mL to 43.7±11.0mg/mL, in contralateral control kidneys, and from
542 34.4±11.3mg/mL to 37.6±9.7mg/mL from day 1 to day 25 post-IRI in ischemic kidneys (**Fig. 5M**).
543 However, the comparative lack of brush borders at early time points (pre-day 5 post-IRI) may have
544 caused a skewing of these analyses towards 'less-perturbed' regions that still had brush border present
545 for analysis relative to tubules that entirely lost their brush border and so would be precluded from
546 this analysis. All these features displayed highly significant time effects from day 1 to 25 post-IRI (*two-*

547 *way ANOVA time effect*: $p \leq 0.0001$; **Fig. 5J–M**). Not surprisingly, there were significant interaction
548 effects (all $p \leq 0.0001$) between contralateral control and ischemic kidneys at each timepoint for each
549 of the four anatomical regions quantified in Panels J–M, showing differential effects of ischemia on
550 contralateral control and ischemic kidneys.

551 To understand the power of the quantitative nature of NoRI data when combined with CNNs we
552 examined kidneys from day 2 post-IRI for deeper analysis. We found a considerable improvement in
553 F1-scores (as a measure of accuracy of predicting ischemic from contralateral control kidney images)
554 when we utilized both protein and lipid versus just protein alone (F1=0.84 *versus* 0.99, respectively).
555 This gave us our first sense of the importance of the lipid information, which cannot be studied using
556 conventional histology techniques since lipids are extracted during the embedding procedure. We
557 expanded these analyses by asking how important the absolute quantitative information obtained by
558 NoRI was, compared with less quantitative measurements, for the simple task of distinguishing
559 contralateral control from ischemic kidneys at day 2 post-IRI. To make this comparison we generated
560 non-quantitative NoRI images where samples were normalized on a per-image basis, and protein and
561 lipid were also normalized in isolation from one another (similar to intensity-based histogram
562 adjustments in conventional histology). As expected, there was a reduction in F1-scores from
563 quantitative to non-quantitative data, with a further drop between non-quantitative data when only
564 protein is used compared to protein and lipid together (**Supplementary Fig. 13**).

565 **Discussion**

566 NoRI is a novel microscopy technique that provides a highly quantitative measure of both protein and
567 lipid biomass concentrations at high spatial resolution. As such it represents a potentially powerful
568 new tool for detecting subtle tissue injury or physiological state change. This is the *a priori* argument,
569 but it is only in the setting of real pathology that one can assess the value of any new histopathological
570 method. Hence, our goal in this study was to test NoRI on a realistic problem of tissue physiology; we
571 chose ischemic reperfusion injury in the kidney. We found that in the setting of fully quantitative,
572 spatial information where there was no disturbance to tissue architecture, as provided by NoRI, we
573 were able to characterize, and for the first time, quantitate known features of AKI (e.g., luminal protein
574 plugs and brush border loss), and discover novel features of kidney damage and reparative processes
575 that would not have been possible previously (e.g., lipid droplet concentration heterogeneity, brush
576 border lipid concentrations). Further, we found that precisely because NoRI images are fully
577 quantitative, normalised to a reference calibration on each day of use, and do not require tissue
578 processing, and hence do not cause disruption of tissue architecture, they are fully reproducible. As
579 such, they are the ideal image data for analysis by neural networks. This combination of advanced,
580 unbiased analysis methods, such as with NoRI images, can provide a unique platform to explore and
581 identify previously unknown biological phenomena in the setting of complex tissues, and at the same
582 time to compare the effectiveness of different methods to do so.

583 The standard protocols in histopathology involve fixation, dehydration, generally paraffin embedding,
584 and sectioning. These processes extract lipids, which represent a considerable portion of mammalian
585 cellular biomass. Routine clinical pathology uses an array of techniques, such as stains like hematoxylin
586 and eosin, most recently complemented by immunohistochemistry, usually on microtome-cut,
587 paraffin-embedded tissue slices. Owing to such harsh treatments required by the needs to preserve
588 some tissue architecture and the hardening of tissue that can then be sectioned to thicknesses of less
589 than 10µm, there is only partial preservation of the *in vivo* architecture. These sequential preparation
590 steps are also time-intensive (as much as several days), and the indirect staining/probing methods

591 exhibit day-to-day variability. As such, while relatively inexpensive, the traditional methods provide an
592 incomplete and imperfect record of tissue architecture. Conversely, the imaging and analytical work,
593 built upon our initial work using NoRI(3), overcomes most of the traditional constraints. Indeed, NoRI
594 is performed in thick (100–500µm, and perhaps up to 1mm) tissue samples that are optically
595 sectioned, rather than mechanically sliced (with an axial resolution of approximately 1.9µm(3)). This
596 allows 3-dimensional high-resolution imaging of cells and organelles and notably does not require
597 tissue processing. It can be performed on formaldehyde-fixed, unfixed or living material(3, 4). It can
598 provide a fully quantitative readout of protein and lipid concentrations, and, by varying the
599 wavelength, can distinguish chemical differences, such as the degree of saturation of lipids and the
600 quantitative levels of cholesterol. With proper protocols in place (i.e., where appropriate machine
601 learning models have been trained prior), imaging and analysis can be performed in <1 hour of tissue
602 presentation. Furthermore, NoRI is fully compatible with immunofluorescence.

603 As discussed above, NoRI images can be processed quickly (<1 hour) compared to conventional
604 histology (hours-to-days). Once acquired, we have developed protocols for automatically segmenting
605 kidney tubules and substructures (nuclei, nucleoli, brush border, lumen) using two open-access
606 methods—SAM and YOLO v.8—that performed with high precision when compared with laboriously
607 obtained hand-segmented reference data. This unexpected facility can largely be explained by the
608 reproducibility and quantitative nature of NoRI data. Spectrophotometric detection of optimally
609 sectioned material is computationally unmixed to offset any impact of light scattering in complex
610 samples. After trying many computation methods, we settled on an open-access convolutional neural
611 network (ResNet50); it provided a powerful and fast means of high-dimensional analysis of NoRI
612 image. Indeed, we have shown how, with very little input training data (as few as 2–3 input images),
613 we are able to identify three distinct tubule types, anatomical location, biological sex, and disease
614 status of tubules with high confidence. While cytoplasmic protein and lipid concentrations were
615 sufficient to delineate proximal from distal tubules with reasonable confidence, the use of protein,
616 lipid, and geometric data in the ResNet50 pipeline was able to determine different tubule types with

near-perfect (against the gold standard of human annotation) certainty. We further discovered the context-specific importance of lipid and protein concentrations during this process. For example, we found that lipids were the most important feature to distinguish contralateral control from ischemic kidneys at day 2 post-IRI, suggesting lipids are central to the early pathology of acute tubular injury. Conversely, protein concentrations were a stronger determinant of predicting the sex of the kidney being analysed, indicating lipid handling within the kidney is more congruent between male and female tubules than is protein. These results importantly show the value of NoRI quantification of both proteins and lipids.

Another important characteristic of the quantitative protein and lipid data obtained by NoRI, coupled with the preservation of tissue architecture due to the lack of tissue processing required for NoRI, was the ability to detect small structures of importance in these images. This was made most clear when we applied the same machine learning analysis approaches to both NoRI and H&E sections from the same male and female mice for direct comparison. The value of this finding is in support of the lack of sample processing, and thereby greater preservation of *in situ* tissue architecture with NoRI imaging compared to conventional histology techniques. Using NoRI image data, the neural network models we developed were able to identify, consistently, small and refined structures such as lipid droplets to distinguish males from females. Comparatively, H&E images, analysed using the same approaches, were unable to identify the sex of the kidney from quantitation of such small structures, and instead only identified larger structures, such as tubules, as distinguishing features of male and female kidneys. This side-by-side comparison of NoRI *versus* H&E in the same specimens highlighted that, when combining NoRI with these advanced analysis techniques, we were uniquely positioned to make striking insights into healthy and diseased mouse kidneys.

The utility of NoRI in histology and pathology

641 We chose the kidney as a model system for testing the effectiveness of NoRI, combined with neural
642 networks/machine learning methods for the analyses of tissue histology and/or pathology. The kidney
643 is comprised of highly repeated structures (tubules), distinct anatomical characteristics
644 (cortex/medulla), distinct sub-structures (cytoplasm, brush border, lumens), and a variety of cell types.
645 With these attributes in mind, we addressed three biological questions: the extent and nature of the
646 kidney's anatomical variability, its sexual dimorphism, and anatomical changes in the response to
647 ischemia-reperfusion injury (as a model of Acute Kidney Injury [AKI]).

648 Using NoRI alone we found distinct clustering of cell types solely by their concentration of protein and
649 lipid. This was confirmed by the unique expression of transporters and channels revealed by specific
650 antibodies. The distal tubules, proximal tubules, and collecting ducts are epithelial cells expressing
651 different membrane antigens. Yet, unexpectedly, the cytoplasm of proximal tubules was significantly
652 higher in total protein on average by 24mg/mL and lower in lipid on average by 10mgmL. Collecting
653 ducts were lower in both protein and lipid than either proximal or distal tubules by 32-56mg/mL and
654 12-22mg/mL, on average, respectively. What was also notable from these results was how tightly-
655 regulated the cytoplasmic concentrations of proteins and lipids were within tubule types. The protein
656 concentrations varied on average 17.2mg/mL (9.5%), while the lipid concentrations varied 9.9mg/mL
657 (17.2%). We also found that the nuclear protein content varied between tubule types, with proximal
658 tubules having ~30mg/mL higher protein concentrations than distal tubules or collecting ducts. Before
659 NoRI measurements, such information on the distinctive lipid and protein concentrations in the
660 cytoplasm of kidney tubules has not to our knowledge been previously reported. Differential
661 cytoplasmic lipid content between tubule types may be related to metabolic differences, with proximal
662 tubules biased towards lipid metabolism, evidenced by a greater abundance of PPARα/γ—involved in
663 lipid metabolism—while distal tubules are more glycolytic in nature(23), and therefore less reliant on
664 an intracellular lipid pool. The lower cytoplasmic protein density of proximal tubules may be due to
665 their higher lipid content and enhanced rate of lipid oxidation/turnover. Such observations suggest

666 that quantitative features of protein and lipid density may reflect physiological conditions and be more
667 informative than are morphological phenotypes.

668 Having established that we could determine tubule identify with high confidence, we investigated the
669 anatomical variation of the kidney protein and lipid as related to anatomy. We first examined nephrons
670 in three adjacent anatomical regions—Rostral pole, Midpole, and Caudal pole portions—from cortex
671 to medulla.

672 These three regions were easily distinguishable by NoRI, as exemplified by protein concentration
673 difference in the microvasculature, which ranged 77.2—100.2mg/mL, and was almost 30mg/mL
674 higher in Caudal relative to Rostral or Midpole regions. Likewise, lipid droplet concentrations were
675 considerably different between regions, being highest in Caudal pole sections, whereas lipid droplet
676 size was nearly 3-fold greater in Midpole regions relative to Rostral and Caudal pole sections. These
677 results represent an intriguing insight into the kidney microvasculature. Prior work utilising super-
678 resolution ultrasound imaging in Zucker rats identified the Midpole as the region most dense in
679 microvasculature(24), while we found protein concentration was greatest in the Caudal pole region.
680 This may, of course, represent a species difference that remains to be determined, but may also
681 represent a subtle difference in the microvasculature itself. For instance, should microvasculature be
682 most dense in the Midpole region—as suggested by McDermott*, et al.* (24)—the endothelial cells
683 themselves may have differential cytoplasmic protein concentrations, reflecting the higher Caudal
684 protein concentrations relative to Midpole or Rostral pole regions in the present study.

685 It is well-known that mouse kidneys exhibit some degree of sexual dimorphism, with larger kidneys in
686 males, reflecting differential water and sodium transporter expression(25-27). Human male and
687 female kidneys show different rates of decline in function with age(27), differential endothelial
688 integrity, differential metabolic profiles, and divergent responses to ischemic-reperfusion injury
689 (*summarized in* Steiger*, et al.* (28)). These differences are most pronounced in the cortex and outer
690 stripe of the medulla(29). Consistent with these findings, we were easily able to distinguish male from

691 female kidneys at a structural level with high reproducibility in the NoRI images. On the compositional
692 level, we found cytoplasmic protein content was significantly higher in proximal tubules from female
693 mice (256.9±6.9mg/mL) *versus* males (245.5±3.2mg/mL). By contrast, cytoplasmic lipid was more
694 concentrated across all tubules in female mice (males: 50.2±2.0mg/mL *versus* females:
695 57.1±2.5mg/mL), which could be consistent with the higher resilience to lipid accumulation in female
696 relative to male kidneys(30). This was also supported by another feature: our finding that lipid droplets
697 were, on average, almost 7.2μm^3 larger in female kidneys and brush border lipid concentration was
698 11.65mg/mL more concentrated, on average, in females compared to males. Furthermore, the protein
699 content of the nucleus was also, on average 26.3mg/mL higher in female tubules. It is also known that
700 female brush border transporter expression and function also differ from males, which may be partially
701 androgen-related(30, 31). While the molecular basis underlying molecular differences in the protein
702 content of the nucleus is unknown and the reasons for the much greater lipid density in female brush
703 borders remain uncertain, these findings show that there are several sexual dimorphisms in murine
704 kidneys, which NoRI has been able to provide the first quantitative readouts for. The power of such
705 quantitative measurements by NoRI is significant. Further, we have also shown how, using NoRI
706 coupled with neural network analyses, we can delineate these sexual dimorphisms in regions as small
707 as 16.6μm^2, with ≥85% certainty, emphasizing the pervasive and consistent characteristics of sexual
708 dimorphism in the kidney

709 With this morphological and structural consistency in mind, we applied NoRI to the ischemic-
710 reperfusion injury model of kidney dysfunction and repair that resembles AKI in humans(22, 31, 32).
711 We can replicate the natural event by transiently interrupting the blood supply to one kidney via
712 clamping the renal artery leaving the contralateral kidney unperturbed directly. As discussed further
713 below, we initially assumed the unperturbed kidney would act as a convenient internal contralateral
714 control. The ensuing hypoxia, caused by a transient clamping of the renal artery leads to both acute
715 functional and structural injury to the ligated kidney, and following 25 days from injury, the kidney
716 recovers much of its function and repairs the damage. Histologically, the transient damage results in

717 sporadic patches of injured tubules and necrosis, characterised by protein plugs in the luminal regions
718 and loss of brush borders. During the recovery phase there are morphologically distinct recovering
719 tubules, and seemingly spared healthy tubules(32). It is known that the relative abundance of these
720 damaged and healthy regions depends on the ischemia duration, age, sex, and underlying disease(32).
721 Ischemic injury is known to cause both endothelial and epithelial cell breakdown and swelling(22),
722 which would likely explain the features identified in NoRI images. The accumulation of protein within
723 the inter-tubule regions may perhaps also be reflective of an accumulation of leukocytes and
724 fibroblasts around dead/dying tubules as part of the adaptive response to injury(22, 31, 32), especially
725 in male kidneys(33). We also found day 2 post-injury was hallmarked by differences in lipid droplet
726 concentrations (on average 16mg/mL higher in ischemic relative to contralateral control kidneys) in
727 proximal tubules. Specifically, we observed a steady increase in both protein and lipid within brush
728 border regions by day 25 post-injury relative to day 1 with an average increase of 8.3mg/mL and
729 3.1mg/mL protein, and 16.2mg/mL and 1.1mg/mL lipid concentration in contralateral and ischemic
730 kidneys, respectively. This likely represents the re-establishment of the brush border (more marked in
731 contralateral control than ischemic kidneys).

732 The large changes in lipid amount and distribution suggest that metabolic changes are a central feature
733 of ischemic reperfusion injury. For example, as discussed above, we identified lipid droplet
734 concentrations, and heterogeneity in droplet concentration, as well as brush border lipid
735 concentrations as major determinants of the injury and repair process during this model of AKI. Kidney
736 proximal tubules are heavily reliant on fatty acid oxidation as a primary source of energy production.
737 Defective lipid handling is a hallmark of renal dysfunction and fibrosis(34, 35). It is, therefore,
738 interesting to quantitatively capture distinct changes in lipid droplet concentrations following ischemic
739 injury in both contralateral control and ischemic kidneys, within their spatial context. These
740 observations are greatly facilitated by NoRI given it provides the first quantitative readout of total lipids
741 in AKI, as lipotoxicity is established as a major hallmark of AKI, and a focus of therapeutic
742 developments(35). Lipid droplets are a heterogeneous population of phospholipid monolayer-bound

743 organelles that store neutral lipids, usually for later use by metabolic systems(36, 37). When the lipid
744 supply outweighs utilization, a lipid-storage response is initiated(38). Therefore, it could be expected
745 that ischemic injury, which causes substantial impairments to beta-oxidation capacity in tubules and a
746 switch to anaerobic metabolism(38, 39) would lead to substantial lipid accumulation. The transport of
747 lipid from the blood might be unlinked from the utilization of lipid, which requires oxidative respiration,
748 which has been inhibited by hypoxia. This imbalance would be expected to lead to an accumulation of
749 lipid droplets during transient hypoxia. Though this might seem reasonable, we in fact observe just the
750 opposite, a lower lipid droplet concentration in ischemic kidneys relative to contralateral control
751 kidneys, notably at day 2 post-IRI (92.8±22.7 *versus* 76.8±25.8mg/mL for contralateral control and
752 ischemic kidneys, respectively). This trend persisted to day 25 with lipid droplet concentrations being
753 ~6.5 and 9.4mg/mL lower in ischemic relative to contralateral control kidneys. While the density of
754 lipid droplets may change in response to changes in their biophysical properties and constituent lipids
755 (triglycerides, cholesterol esters, fatty acids), the presence of coalesced regions of lipids following
756 ischemic-reperfusion injury may not represent physiological lipid droplets *per se* and instead may
757 represent pools of lipids within the debris of dead/dying cells. Lipid-droplet membrane protein probing
758 by immunofluorescence may clarify this uncertainty in future work. Thus, if this undirected
759 accumulation of lipids occurs from the remnant lipids from within the dead cells' cytoplasm, then their
760 density could feasibly be less than organelle-bound lipids. Indeed, the observation of significantly large
761 lipid droplets by day 5 post-injury could support this suggestion.

762 An important contribution made by NoRI in the context of the reperfusion-injury model of acute
763 kidney injury used here was the profound influence the injury imparted on the contralateral control
764 kidney over time. Our quantitative histopathology investigations of the responses over time in the
765 contralateral control kidneys identified many features of dysfunction and damage. Notably, we were
766 able to distinctly separate individual time points between days 1 to 25 post-IRI in the contralateral
767 control group, specifically, by performing neural network analysis on NoRI images. Specifically, these
768 models highlighted a gradual increase in luminal protein (i.e., protein plugs) from days 1 to 25, as well

769 as a gradual increase in lipid droplet concentrations, similar to what was observed in the ischemic
770 kidneys. Furthermore, by day 25 post-IRI there was a dramatic increase in brush border protein and
771 lipid concentrations in the contralateral control kidneys, relative to days 1–5 post-IRI, suggestive of a
772 re-establishment of the brush border that was previously reduced in size and density in the
773 contralateral control kidneys. Our observations support prior work that show the structural,
774 transcriptional, and functional dysfunction in the contralateral control kidneys of this model of AKI,
775 but crucially add additional, quantitative data to this body of work.

776 The dysfunction in the contralateral control kidneys can be segregated into short-term (hours/days),
777 medium-term (days/weeks), and long-term (weeks/months) post-injury. In the short-term,
778 contralateral control kidneys exhibit strong transcriptional shifts due to oxidative stress, increased
779 inflammatory cytokines, and metabolic dysfunction(40, 41). Indeed, the contralateral kidney is
780 exposed to the cytokine storm and oxidative stress produced by the ischemic-damaged kidney, which
781 can influence the healthy kidney that is responsible for a greater proportion of the biological function
782 of two kidneys. In this context, we found a notable change in lipid droplet concentrations from
783 ~90mg/mL on day 1 post-IRI to ~105mg/mL by day 25. This provides a quantitative measurement
784 supporting and expanding upon previous reports of downregulated lipid metabolism pathways in the
785 contralateral control kidney within 24-hours of injury(42). Our results represent the first highly
786 sensitive, quantitative measurement of lipid-related effects of ischemic-reperfusion injury, to our
787 knowledge. In the weeks following injury, leukocytes, including activated T-cells, infiltrate both kidneys.
788 This can represent both part of the damage-induced inflammatory program as well as the structural
789 remodelling—in concert with fibroblasts—that occurs within the contralateral kidney as it
790 compensates for the loss of the damaged kidney(43). In this respect, our analyses identified several
791 features of both tubule damage/stress and structural remodelling within the contralateral kidney.
792 These were hallmarked by the gradual increase in luminal protein from ~32mg/mL on day-1 to
793 ~40mg/mL on day-25 post-injury. Likewise, brush borders showed quantitative evidence of either re-
794 establishment post-injury, or increased abundance and/or density of structures by day-25 post-injury,

795 evidenced by a dramatic increase in protein (from ~125mg/mL to ~140mg/mL) and lipid (from
796 ~36mg/mL to ~44mg/mL) concentrations at day-25 relative to days 1–5 post-injury. Such quantitative
797 tracking of the micro-anatomy of the kidney in the context of AKI constitutes an exciting development
798 of both known features of kidney damage and repair as well as possibly presenting novel features of
799 injury and repair. These data represent initial insights into the power of NoRI as a tool for making novel
800 biological insights into pathological states, as well as being a useful diagnostic tool in histopathology.

801

802 **Conclusion**

803 We present this first exploration of the potential of NoRI—a fully quantitative normalized form of
804 stimulated Raman spectroscopy that measures protein and lipid content in biological samples—
805 combined with neural network analysis as a tool for feature identification and diagnostics in
806 histopathology. We have shown, using murine kidney as a candidate organ for these investigations,
807 that NoRI is fully capable of analysing complex tissue samples in a way that could be considered
808 superior to conventional histology methods, owing to its comparatively fast turnaround time from
809 sample harvesting to imaging, its ability to analyze samples without the need for destructive or
810 damaging sample processing, and its ability to fully quantify protein and lipids, label-free, at high
811 spatial resolution. Moreover, we have shown how this form of microscopy, due to its absolute (as
812 opposed to relative) quantitation is highly appropriate for analysis by neural networks for feature
813 discovery. Because it is a spectrophotometric absolute measurement, it releases the power of machine
814 learning for unbiased feature discovery, suggesting that it may have strong diagnostic potential in
815 physiology and disease. Finally, due to the reproducibility (both between animals and within tubule
816 types) and the quantitative nature of these data, these advanced analysis approaches require a
817 relatively low level of input data for feature discovery, such that fine-tuned models can be easily
818 derived and applied to related samples. Thus, NoRI could be applied to a vast array of biological
819 questions and disease states to make both novel biological discoveries and facilitate disease
820 diagnostics in the clinical context. Of these questions, both discovery of novel foci, and the early

diagnosis of cancers are fundamental questions that NoRI is well-placed to make advancements in. Likewise, the application of NoRI to the ageing process could add fundamental insights into a poorly understood, biologically relevant phenomenon, especially given the accumulation of lipids in many organs with age, and the fact that senescent cells are characterised by cell swelling and cytoplasmic mass-density uncoupling.

References:

1. B. Bracegirdle, The History of Histology: A Brief Survey of Sources. *History of Science* **15**, 77-101 (1977).
2. O. Bock (2015) A history of the development of histology up to the end of the nineteenth century.
3. S. Oh *et al.*, Protein and lipid mass concentration measurement in tissues by stimulated Raman scattering microscopy. *Proceedings of the National Academy of Sciences* **119**, e2117938119 (2022).
4. X. Liu, S. Oh, M. W. Kirschner, The uniformity and stability of cellular mass density in mammalian cell culture. *Front Cell Dev Biol* **10**, 1017499 (2022).
5. C. W. Freudiger *et al.*, Label-free biomedical imaging with high sensitivity by stimulated Raman scattering microscopy. *Science* **322**, 1857-1861 (2008).
6. A. H. Hill, B. Manifold, D. Fu, Tissue imaging depth limit of stimulated Raman scattering microscopy. *Biomed Opt Express* **11**, 762-774 (2020).
7. N. Suzuki *et al.*, Deep learning-based histopathological assessment of tubulo-interstitial injury in chronic kidney diseases. *Communications Medicine* **5**, 3 (2025).
8. T. T. U. Nguyen *et al.*, Deep-learning model for evaluating histopathology of acute renal tubular injury. *Scientific reports* **14**, 9010 (2024).
9. D. L. Hölscher, R. D. Bülow, M. Strauch, P. Boor, Advances in Computational Nephropathology. *Kidney International* https://doi.org/10.1016/j.kint.2025.06.029 (2025).
10. S. Preibisch, S. Saalfeld, P. Tomancak, Globally optimal stitching of tiled 3D microscopic image acquisitions. *Bioinformatics* **25**, 1463-1465 (2009).
11. R. Karmakar, W. Trim, M. Kirschner, S. Noerrelykke, Kidney Tissue Characterization using Normalized Raman Imaging and Segment-Anything. *bioRxiv* 10.1101/2025.10.09.681509, 2025.2010.2009.681509 (2025).
12. A. Kirillov *et al.* (2023) Segment anything. in *Proceedings of the IEEE/CVF international conference on computer vision*, pp 4015-4026.
13. J. Redmon, S. Divvala, R. Girshick, A. Farhadi (2016) You only look once: Unified, real-time object detection. in *Proceedings of the IEEE conference on computer vision and pattern recognition*, pp 779-788.
14. J. Deng *et al.* (2009) ImageNet: A large-scale hierarchical image database. in *2009 IEEE Conference on Computer Vision and Pattern Recognition*, pp 248-255.
15. S. Berg *et al.*, ilastik: interactive machine learning for (bio)image analysis. *Nature Methods* **16**, 1226-1232 (2019).
16. T. Falk *et al.*, U-Net: deep learning for cell counting, detection, and morphometry. *Nature Methods* **16**, 67-70 (2019).
17. J. Ansel *et al.* (2024) PyTorch 2: Faster Machine Learning Through Dynamic Python Bytecode Transformation and Graph Compilation. in *Proceedings of the 29th ACM International Conference on Architectural Support for Programming Languages and Operating Systems, Volume 2* (Association for Computing Machinery, La Jolla, CA, USA), pp 929–947.
18. D. P. Kingma, J. Ba, Adam: A Method for Stochastic Optimization. *CoRR* **abs/1412.6980** (2014).
19. J. Nunez-Iglesias, R. Kennedy, T. Parag, J. Shi, D. B. Chklovskii, Machine learning of hierarchical clustering to segment 2D and 3D images. *PloS one* **8**, e71715 (2013).

20. K. He, X. Zhang, S. Ren, J. Sun (2016) Deep residual learning for image recognition. in *Proceedings of the IEEE conference on computer vision and pattern recognition*, pp 770-778.
21. R. R. Selvaraju *et al.*, Grad-CAM: Visual Explanations from Deep Networks via Gradient-Based Localization. *International Journal of Computer Vision* **128**, 336-359 (2020).
22. J. V. Bonventre, L. Yang, Cellular pathophysiology of ischemic acute kidney injury. *The Journal of clinical investigation* **121**, 4210-4221 (2011).
23. Z. Lyu *et al.*, PPARγ maintains the metabolic heterogeneity and homeostasis of renal tubules. *eBioMedicine* **38**, 178-190 (2018).
24. A. McDermott *et al.*, Analysing the Renal Vasculature Using Super-Resolution Ultrasound Imaging: Considerations for Clinical and Research Applications. *Diagnostics (Basel)* **15** (2025).
25. S. A. Kalucki *et al.*, Reference values and sex differences in absolute and relative kidney size. A Swiss autopsy study. *BMC Nephrology* **21**, 289 (2020).
26. A. A. McDonough, A. N. Harris, L. Xiong, A. T. Layton, Sex differences in renal transporters: assessment and functional consequences. *Nature Reviews Nephrology* **20**, 21-36 (2024).
27. T. Melsom *et al.*, Sex Differences in Age-Related Loss of Kidney Function. *J Am Soc Nephrol* **33**, 1891-1902 (2022).
28. S. Steiger *et al.*, Sex dimorphism in kidney health and disease: mechanistic insights and clinical implication. *Kidney International* **107**, 51-67 (2025).
29. S. Chen *et al.*, Multi-omic and spatial analysis of mouse kidneys highlights sex-specific differences in gene regulation across the lifespan. *Nature Genetics* **57**, 1213-1227 (2025).
30. F. Juszczak *et al.*, Sex differences in obesity-induced renal lipid accumulation revealed by lipidomics: a role of adiponectin/AMPK axis. *Biol Sex Differ* **14**, 63 (2023).
31. L. C. Veiras *et al.*, Sexual Dimorphic Pattern of Renal Transporters and Electrolyte Homeostasis. *J Am Soc Nephrol* **28**, 3504-3517 (2017).
32. E. E. Hesketh *et al.*, Renal ischaemia reperfusion injury: a mouse model of injury and regeneration. *J Vis Exp* 10.3791/51816 (2014).
33. K. M. Park, J. I. Kim, Y. Ahn, A. J. Bonventre, J. V. Bonventre, Testosterone is responsible for enhanced susceptibility of males to ischemic renal injury. *The Journal of biological chemistry* **279**, 52282-52292 (2004).
34. L. E. Lee, T. Doke, D. Mukhi, K. Susztak, The key role of altered tubule cell lipid metabolism in kidney disease development. *Kidney International* **106**, 24-34 (2024).
35. A. A. Otunla, K. Shanmugarajah, A. H. Davies, J. Shalhoub, Lipotoxicity and immunometabolism in ischemic acute kidney injury: current perspectives and future directions. *Frontiers in Pharmacology* **Volume 15 - 2024** (2024).
36. N. Mejhert *et al.*, The Lipid Droplet Knowledge Portal: A resource for systematic analyses of lipid droplet biology. *Developmental Cell* **57**, 387-397.e384 (2022).
37. A. E. Ventura *et al.*, Cell lipid droplet heterogeneity and altered biophysical properties induced by cell stress and metabolic imbalance. *Biochimica et Biophysica Acta (BBA) - Molecular and Cell Biology of Lipids* **1868**, 159347 (2023).
38. N. Mejhert *et al.*, Partitioning of MLX-Family Transcription Factors to Lipid Droplets Regulates Metabolic Gene Expression. *Mol Cell* **77**, 1251-1264.e1259 (2020).

39. P. Erpicum, P. Rowart, J.-O. Defraigne, J.-M. Krzesinski, F. Jouret, What we need to know about lipid-associated injury in case of renal ischemia-reperfusion. *American Journal of Physiology-Renal Physiology* **315**, F1714-F1719 (2018).
40. H. Fatemikia, F. Ketabchi, Z. Karimi, S. M. S. Moosavi, Distant effects of unilateral renal ischemia/reperfusion on contralateral kidney but not lung in rats: the roles of ROS and iNOS. *Canadian Journal of Physiology and Pharmacology* **94**, 477-487 (2015).
41. T. Möckel, S. Boegel, A. Schwarting, Transcriptome analysis of renal ischemia/reperfusion (I/R) injury in BAFF and BAFF-R deficient mice. *PloS one* **18**, e0291619 (2023).
42. A. M. Scantlebery *et al.*, The dysregulation of metabolic pathways and induction of the pentose phosphate pathway in renal ischaemia-reperfusion injury. *The Journal of pathology* **253**, 404-414 (2021).
43. D. P. Basile, E. C. Leonard, D. Tonade, J. L. Friedrich, S. Goenka, Distinct effects on long-term function of injured and contralateral kidneys following unilateral renal ischemia-reperfusion. *Am J Physiol Renal Physiol* **302**, F625-635 (2012).

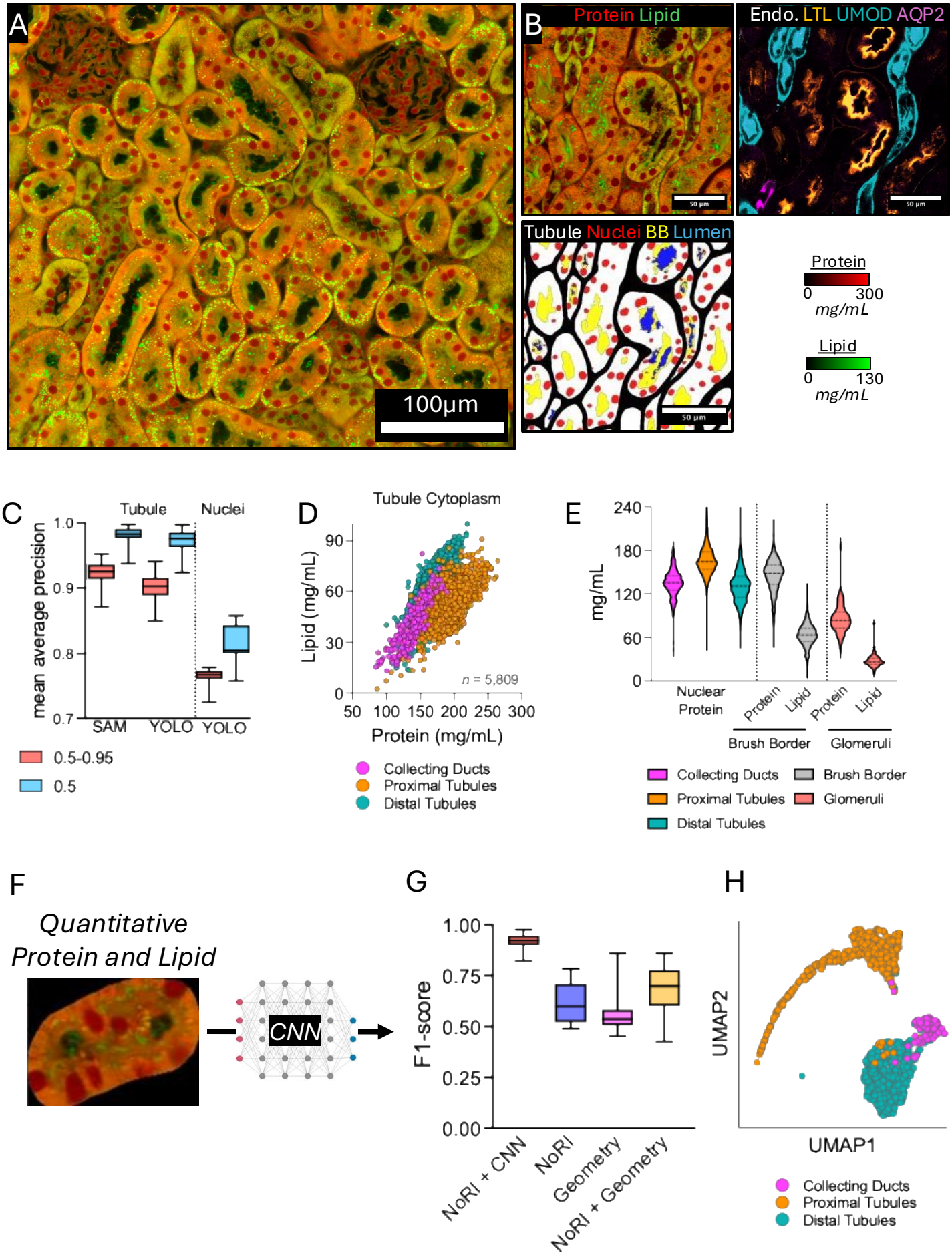
A
100µm
B
Protein Lipid
Endo. LTL UMOD AQP2
Tubule Nuclei BB Lumen
50 µm
Protein
0 300
mg/mL
Lipid
0 130
mg/mL
C
Tubule
Nuclei
mean average precision
1.0
0.9
0.8
0.7
SAM
YOLO
YOLO
0.5-0.95
0.5
D
Tubule Cytoplasm
Lipid (mg/mL)
90
60
30
0
50 100 150 200 250 300
Protein (mg/mL)
n = 5,809
Collecting Ducts
Proximal Tubules
Distal Tubules
E
mg/mL
240
180
120
60
0
Nuclear Protein
Protein
Lipid
Protein
Lipid
Brush Border
Glomeruli
Collecting Ducts
Proximal Tubules
Distal Tubules
Brush Border
Glomeruli
F
Quantitative Protein and Lipid
CNN
G
F1-score
1.00
0.75
0.50
0.25
0.00
NoRI + CNN
NoRI
Geometry
NoRI + Geometry
H
UMAP2
UMAP1
Collecting Ducts
Proximal Tubules
Distal Tubules

Figure 1. Overview of the use of NoRI and CNNs in mouse kidneys

A, Representative NoRI image of mouse kidney. Quantitative readouts of Protein (Red) and Lipid (Green) are displayed. Scale bars representing quantitative protein and lipid signals are presented to the right.

B, Sub-section of mouse kidney simultaneously imaged by NoRI (Left) and immunofluorescence (Right) for tubule type identification, with a representative segmentation mask (Bottom) for tubules, nuclei, brush border, and lumen.

C, Box-whisker plots of mean average precision (0.5 and 0.5-0.95) scores for tubules and nuclei using SAM and YOLOv.8. Scores are relative to hand segmentation of the same structures. Boxes represent median with $25^{th}/75^{th}$ percentiles. Whiskers represent min-to-max values.

D, Scatter plot of cytoplasmic protein and lipid content on a per-tubule basis for two (1x5 mm) kidney sections representing cortex to medulla from the Midpole portion of the left kidney. Color labels for tubule types were assigned according to immunofluorescence staining.

E, Violin plot of nuclear protein, brush border, and glomeruli protein and lipid content on a per-tubule basis for tubules also displayed in Panel D. Data represent a total of 1,662 tubules. Violins are presented with median (dashed line) and $25^{th}/75^{th}$ percentiles (dotted lines).

F, Representative NoRI image of a single tubule analysed by ResNet50 for tubule-type identification by NoRI images without immunofluorescence.

G, Box-whisker plots of F1-scores for tubules input into ResNet50 for tubule prediction. Comparisons between ResNet50 (CNN + NoRI) analyses is presented against each module within the data, including protein and lipid data alone (NoRI), Geometry only, and NoRI+Geometry. Boxes represent median with $25^{th}/75^{th}$ percentiles. Whiskers represent min-to-max values.

H, UMAP plot of tubules clustered by ResNet50. Color coding represents tubule identification assigned by immunofluorescence. Each datapoint represents an individual tubule.

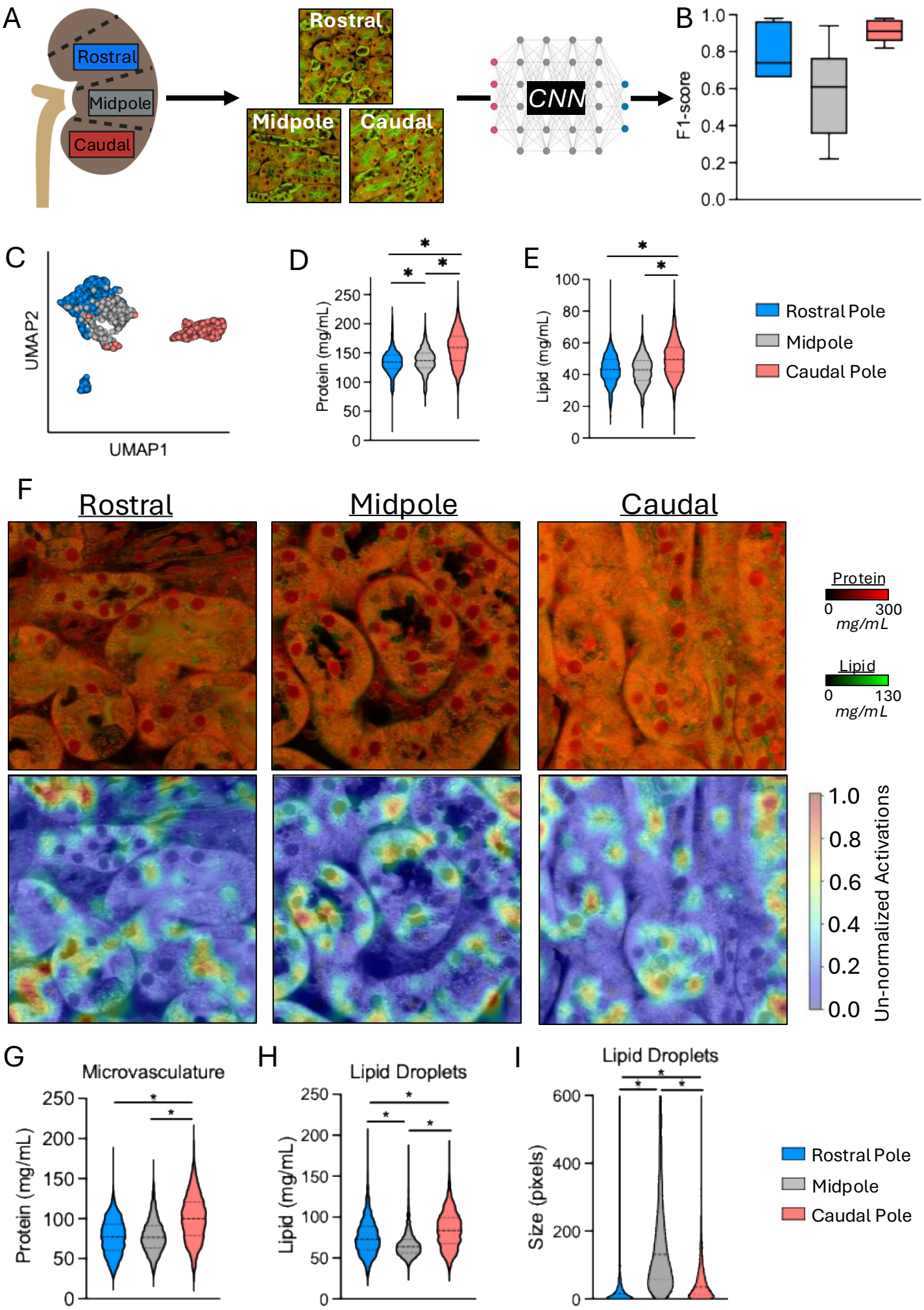
A
Rostral
Midpole
Caudal
Rostral
Midpole
Caudal
CNN
B
F1-score
1.0
0.8
0.6
0.4
0.2
0.0
C
UMAP2
UMAP1
D
Protein (mg/mL)
250
200
150
100
50
0
E
Lipid (mg/mL)
100
80
60
40
20
0
Rostral Pole
Midpole
Caudal Pole
F
Rostral
Midpole
Caudal
Protein
0
300
mg/mL
Lipid
0
130
mg/mL
1.0
0.8
0.6
0.4
0.2
0.0
Un-normalized Activations
G
Microvasculature
Protein (mg/mL)
H
Lipid Droplets
Lipid (mg/mL)
I
Lipid Droplets
Size (pixels)
600
400
200
0
Rostral Pole
Midpole
Caudal Pole

Figure 2. Exploration of kidney anatomy by NoRI.

A, Schematic of experimental design, wherein 2-3 kidney sections from three distinct anatomical regions were imaged by NoRI and input into ResNet50.

B, Box-whisker plots of F1-scores for anatomical region prediction on a per-tubule basis. Boxes represent median with $25^{th}/75^{th}$ percentiles. Whiskers represent min-to-max values.

C, UMAP plot of tubules color coded by anatomical region predicted by ResNet50. Each datapoint represents an individual tubule.

D, Violin plots of tubule cytoplasmic protein content measured by NoRI, split by anatomical region. Violins are presented with median (dashed line) and $25^{th}/75^{th}$ percentiles (dotted lines).

E, Violin plots of tubule cytoplasmic lipid content measured by NoRI, split by anatomical region. Violins are presented with median (dashed line) and $25^{th}/75^{th}$ percentiles (dotted lines).

F, Representative NoRI images from each anatomical region with heatmap of features defining each region identified by ResNet50.

G, Violin plot of microvasculature protein concentration identified by ResNet50 between anatomical regions. Violins are presented with median (dashed line) and $25^{th}/75^{th}$ percentiles (dotted lines).

H, Violin plot of lipid droplet lipid concentration identified by ResNet50 between anatomical regions. Violins are presented with median (dashed line) and $25^{th}/75^{th}$ percentiles (dotted lines).

I, Violin plot of lipid droplet size (in pixels) identified by ResNet50 between anatomical regions. Violins are presented with median (dashed line) and $25^{th}/75^{th}$ percentiles (dotted lines).

Statistical comparisons in Panels D, E, G–I were performed using Kruskal-Wallis tests with Dunn's post-hoc corrections applied.

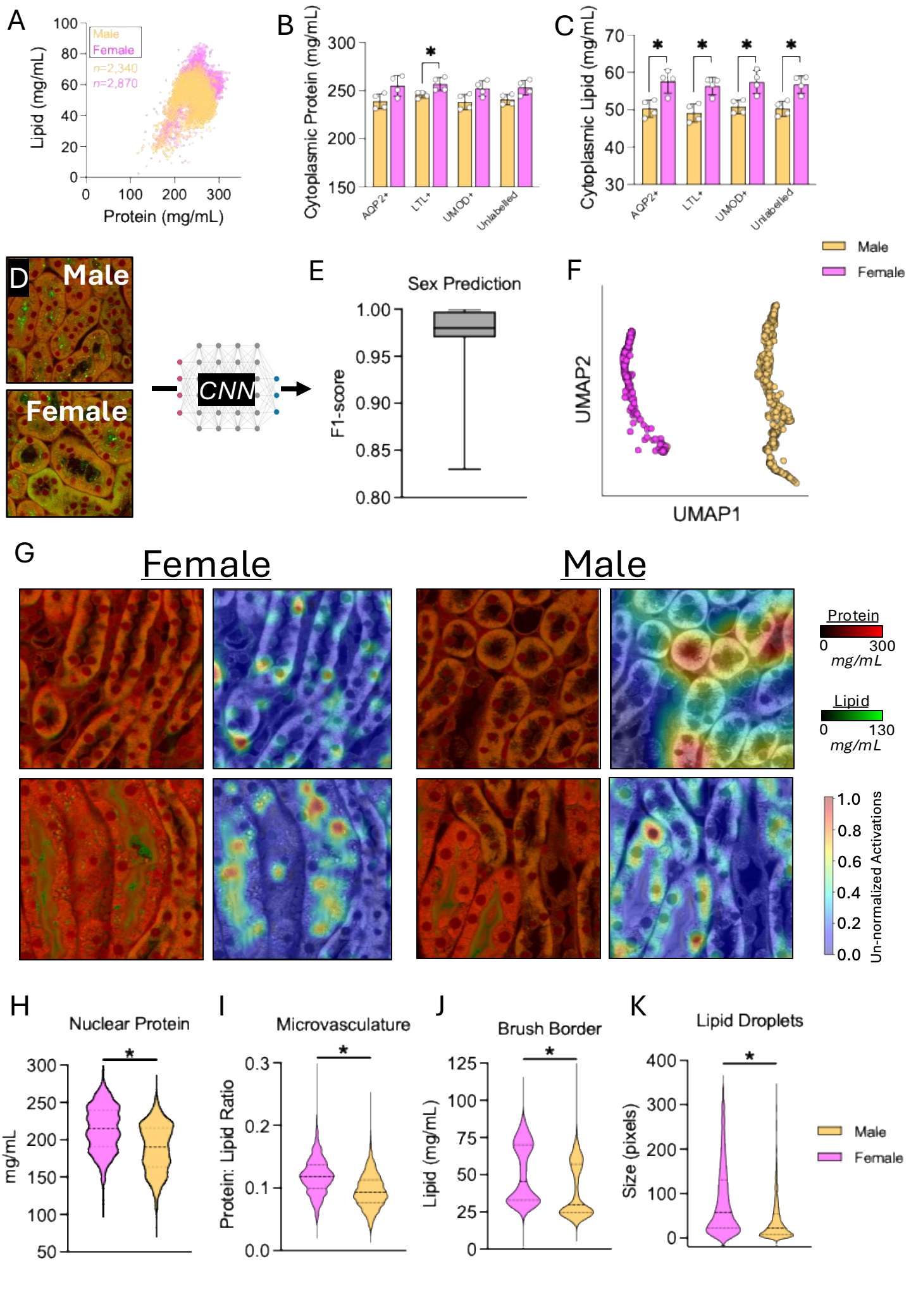
A
Male
Female
n=2,340
n=2,870
Lipid (mg/mL)
Protein (mg/mL)
B
Cytoplasmic Protein (mg/mL)
AQP2+
LTL+
UMOD+
Unlabelled
C
Cytoplasmic Lipid (mg/mL)
Male
Female
D
Male
Female
CNN
E
Sex Prediction
F1-score
F
UMAP2
UMAP1
G
Female
Male
Protein
mg/mL
Lipid
mg/mL
Un-normalized Activations
H
Nuclear Protein
mg/mL
I
Microvasculature
Protein: Lipid Ratio
J
Brush Border
Lipid (mg/mL)
K
Lipid Droplets
Size (pixels)
Male
Female

Figure 3. Exploration of kidney sex differences by NoRI.

A, Scatter plot of tubule cytoplasmic protein and lipid content measured by NoRI in male and female kidneys (*n* = 4 mice per group). Each datapoint represents an individual tubule.

B, Bar graph of cytoplasmic protein content, split by tubule type, measured by NoRI in male and female kidneys. Each datapoint represents the mean value across all tubules for an individual mouse.

C, Bar graph of cytoplasmic lipid content, split by tubule type, measured by NoRI in male and female kidneys. Each datapoint represents the mean value across all tubules for an individual mouse.

D, Representative NoRI images from male and female mouse kidneys input into ResNet50 for sex prediction on a per-tubule basis.

E, Box-whisker plots of F1-scores for sex prediction on a per-tubule basis from NoRI images. Boxes represent median with $25^{th}/75^{th}$ percentiles. Whiskers represent min-to-max values.

F, UMAP plot of tubules color coded by sex and tubule type predicted by ResNet50. Each datapoint represents an individual tubule.

G, Heatmap figures of female and male kidneys imaged by NoRI representing regions discriminating male from female kidneys according to ResNet50.

H, Violin plot of nuclear protein concentrations identified by ResNet50 between sexes. Violins are presented with median (dashed line) and $25^{th}/75^{th}$ percentiles (dotted lines).

I, Violin plot of microvasculature protein: lipid ratio identified by ResNet50 between sexes. Violins are presented with median (dashed line) and $25^{th}/75^{th}$ percentiles (dotted lines).

J, Violin plot of brush border lipid concentration identified by ResNet50 between sexes. Violins are presented with median (dashed line) and $25^{th}/75^{th}$ percentiles (dotted lines).

K, Violin plot of lipid droplet size (in pixels) identified by ResNet50 between sexes. Violins are presented with median (dashed line) and $25^{th}/75^{th}$ percentiles (dotted lines).

Statistical comparisons in Panels B and C were performed using Kruskal-Wallis tests with Dunn's post-hoc corrections applied. Data in Panels H–K were analysed by Kolmogorov-Smirnov tests.

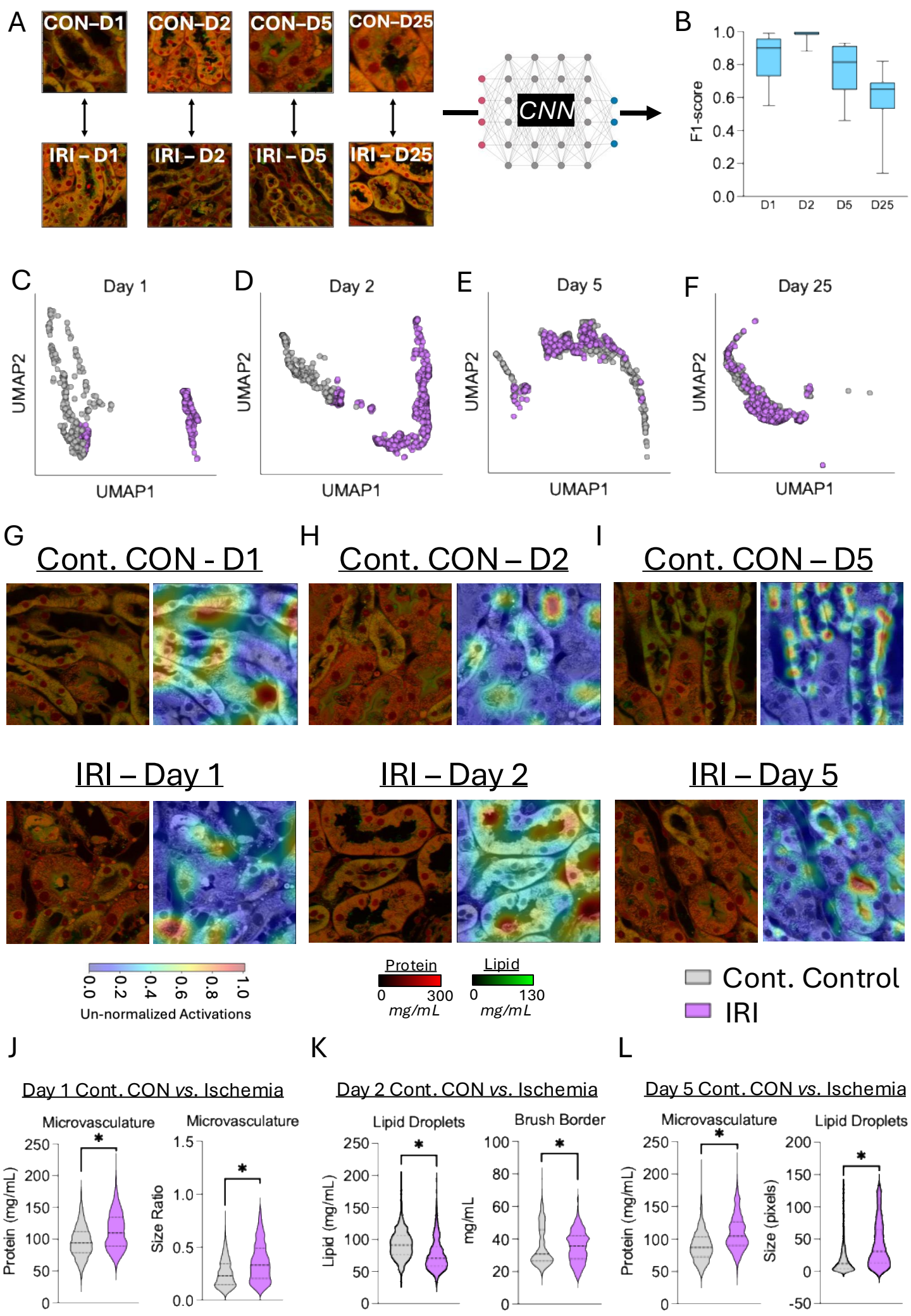
A
CON–D1
CON–D2
CON–D5
CON–D25
IRI – D1
IRI – D2
IRI – D5
IRI – D25
CNN
B
F1-score
1.0
0.8
0.6
0.4
0.2
0.0
D1
D2
D5
D25
C
Day 1
D
Day 2
E
Day 5
F
Day 25
UMAP2
UMAP1
G
Cont. CON - D1
H
Cont. CON – D2
I
Cont. CON – D5
IRI – Day 1
IRI – Day 2
IRI – Day 5
0.0
0.2
0.4
0.6
0.8
1.0
Un-normalized Activations
Protein
0
300
mg/mL
Lipid
0
130
mg/mL
Cont. Control
IRI
J
Day 1 Cont. CON vs. Ischemia
Microvasculature
Protein (mg/mL)
Microvasculature
Size Ratio
K
Day 2 Cont. CON vs. Ischemia
Lipid Droplets
Lipid (mg/mL)
Brush Border
mg/mL
L
Day 5 Cont. CON vs. Ischemia
Microvasculature
Protein (mg/mL)
Lipid Droplets
Size (pixels)

Figure 4. Exploration of the time-course effects of kidney ischemic reperfusion injury by NoRI

A, Representative NoRI images from each time point following ischemic reperfusion injury in both contralateral control (CON) and ischemic (IRI) kidneys input into ResNet50.

B, Box-whisker plots of F1-scores for prediction of contralateral control vs IRI kidneys at each time point post-injury by ResNet50. Boxes represent median with $25^{th}/75^{th}$ percentiles. Whiskers represent min-to-max values.

C, UMAP plot of Cont. CON (contralateral control) (Grey) and IRI (Purple) tubules at day 1 post-injury predicted by ResNet50. Each datapoint represents an individual tubule.

D, UMAP plot of Cont. CON (contralateral control) (Grey) and IRI (Purple) tubules at day 2 post-injury predicted by ResNet50. Each datapoint represents an individual tubule.

E, UMAP plot of Cont. CON (contralateral control) (Grey) and IRI (Purple) tubules at day 5 post-injury predicted by ResNet50. Each datapoint represents an individual tubule.

F, UMAP plot of Cont. CON (contralateral control) (Grey) and IRI (Purple) tubules at day 25 post-injury predicted by ResNet50. Each datapoint represents an individual tubule.

G, Representative NoRI images from Cont. CON (contralateral control) and IRI kidneys at day 1 post-injury with adjacent heatmap of features defining CON from IRI identified by ResNet50.

H, Representative NoRI images from Cont. CON (contralateral control) and IRI kidneys at day 2 post-injury with adjacent heatmap of features defining CON from IRI identified by ResNet50.

I, Representative NoRI images from Cont. CON (contralateral control) and IRI kidneys at day 5 post-injury with adjacent heatmap of features defining Cont. CON (contralateral control) from IRI identified by ResNet50.

J, Violin plots of microvasculature protein content and size measured by NoRI between Cont. CON (contralateral control) and IRI on day 1 post-injury. Violins are presented with median (dashed line) and $25^{th}/75^{th}$ percentiles (dotted lines).

K, Violin plots of lipid droplet concentration and brush border lipid concentration measured by NoRI between Cont. CON (contralateral control) and IRI on day 2 post-injury. Violins are presented with median (dashed line) and $25^{th}/75^{th}$ percentiles (dotted lines).

L, Violin plots of microvasculature protein concentration and lipid droplet size measured by NoRI between Cont. CON (contralateral control) and IRI on day 5 post-injury. Violins are presented with median (dashed line) and $25^{th}/75^{th}$ percentiles (dotted lines).

Data in Panels J–L were analysed by Kolmogorov-Smirnov tests.

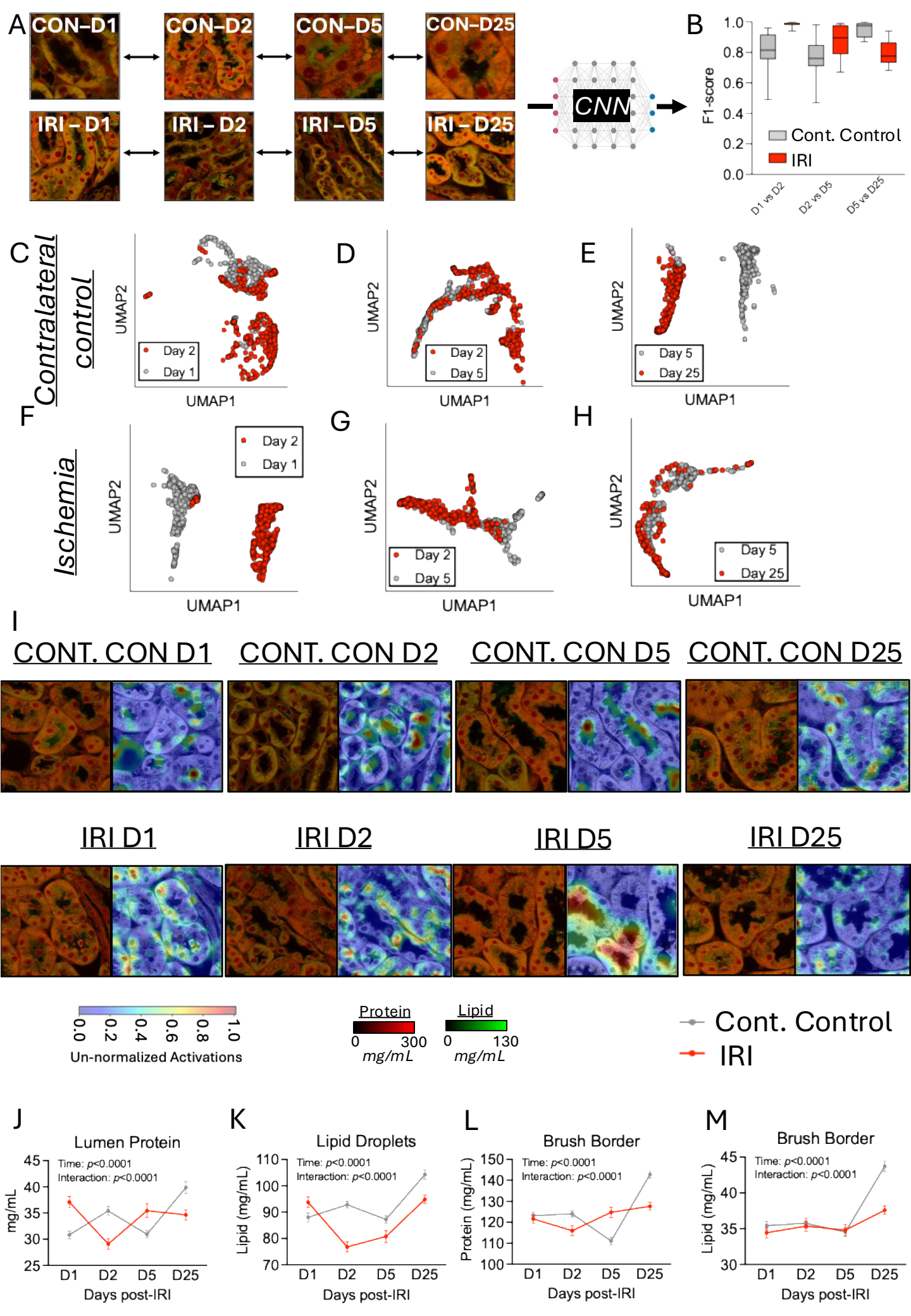
A
CON–D1
CON–D2
CON–D5
CON–D25
IRI – D1
IRI – D2
IRI – D5
IRI – D25
CNN
B
F1-score
Cont. Control
IRI
D1 vs D2
D2 vs D5
D5 vs D25
C
D
E
F
G
H
Contralateral control
Ischemia
UMAP1
UMAP2
Day 2
Day 1
Day 5
Day 25
I
CONT. CON D1
CONT. CON D2
CONT. CON D5
CONT. CON D25
IRI D1
IRI D2
IRI D5
IRI D25
Un-normalized Activations
Protein
Lipid
mg/mL
Cont. Control
IRI
J
Lumen Protein
K
Lipid Droplets
L
Brush Border
M
Brush Border
Time: p<0.0001
Interaction: p<0.0001
mg/mL
Lipid (mg/mL)
Protein (mg/mL)
Days post-IRI

Figure 5. Time course analysis of the effects of ischemic reperfusion injury within contralateral control and IRI kidneys.

A, Representative NoRI images from each time point following ischemic reperfusion injury in both contralateral control (CON) and ischemic (IRI) kidneys input into ResNet50.

B, Box-whisker plots of F1-scores for prediction of the time point post-injury for Cont. Control (contralateral control) and IRI by ResNet50. Boxes represent median with $25^{th}/75^{th}$ percentiles. Whiskers represent min-to-max values.

C, UMAP plot of day 1 (grey) and day 2 (red) tubules for CON kidneys post-injury predicted by ResNet50. Each datapoint represents an individual tubule.

D, UMAP plot of day 2 (grey) and day 5 (red) tubules for CON kidneys post-injury predicted by ResNet50. Each datapoint represents an individual tubule.

E, UMAP plot of day 5 (grey) and day 25 (red) tubules for CON kidneys post-injury predicted by ResNet50. Each datapoint represents an individual tubule.

F, UMAP plot of day 1 (grey) and day 2 (red) tubules for IRI kidneys post-injury predicted by ResNet50. Each datapoint represents an individual tubule.

G, UMAP plot of day 2 (grey) and day 5 (red) tubules for IRI kidneys post-injury predicted by ResNet50. Each datapoint represents an individual tubule.

H, UMAP plot of day 5 (grey) and day 25 (red) tubules for IRI kidneys post-injury predicted by ResNet50. Each datapoint represents an individual tubule.

I, Representative NoRI images from CONT. CON (contralateral control) and IRI kidneys at days 1, 2, 5, and 25 post-injury with adjacent heatmap of features defining each time point, within CON and IRI kidneys identified by ResNet50.

J, Line graph of lumen protein concentration measured by NoRI at each time point post-injury for CONT. CON (contralateral control) (grey) and IRI (red). The mean value for each group at a given time point post-injury is presented, with error bars representing SEM.

K, Line graph of lipid droplet concentration measured by NoRI at each time point post-injury for CONT. CON (contralateral control) (grey) and IRI (red). The mean value for each group at a given time point post-injury is presented, with error bars representing SEM.

L, Line graph of brush border protein concentration measured by NoRI at each time point post-injury for CONT. CON (contralateral control) (grey) and IRI (red). The mean value for each group at a given time point post-injury is presented, with error bars representing SEM.

M, Line graph of brush border lipid concentration measured by NoRI at each time point post-injury for CONT. CON (contralateral control) (grey) and IRI (red). The mean value for each group at a given time point post-injury is presented, with error bars representing SEM.

Data in Panels J-M were analysed by two-way repeated measured ANOVA with Bonferroni post-hoc corrections applied.